

## Chapter 5

# Photonic crystals and light focusing

### 5.1 One- and two-dimensional photonic crystals

Photonic crystals (PCs) [1,2] are the structures with nanoresolution and periodic modulation of the refractive index, which have a photonic band gap. Band gaps define the frequency of electromagnetic radiation, which can not exist in this structure. For optical PCs at a wavelength of  $1.3 \mu\text{m}$  the size of the band gap equals tens of nanometers. Accordingly, total reflection is observed in the fall of electromagnetic radiation on the PC, the frequency of which lies in the band gap. This property determines the prospects of using photonic-crystal structures as waveguides, antireflection coatings, frequency filters, metamaterials, photonic crystal lens, working at a given light frequency.

#### 5.1.1. Photonic band gaps

Based on the general theory of light propagation in the PC [3], we consider the solution of Maxwell's equations for a dielectric medium without free charges and currents which simulates the photonic crystal. The system of Maxwell's equations in this case has the following form (in the CGSE system):

$$\begin{cases} \nabla \mathbf{D} = 0, \\ \nabla \mathbf{B} = 0, \\ \nabla \times \mathbf{E} = -\frac{\partial \mathbf{B}}{\partial t}, \\ \nabla \times \mathbf{H} = \frac{\partial \mathbf{D}}{\partial t}, \end{cases} \quad (5.1)$$

where  $\mathbf{D} = \varepsilon \varepsilon_0 \mathbf{E}$ ,  $\mathbf{B} = \mu \mu_0 \mathbf{H}$ ,  $\sqrt{(\varepsilon_0 \mu_0)^{-1}} = c$ ,

From (5.1) we obtain the following relation:

$$\varepsilon^{-1}(r)(\nabla \times \mathbf{H}) = \varepsilon_0 \frac{\partial \mathbf{E}}{\partial t}. \quad (5.2)$$

Applying the ‘rot’ operation to the expression (5.2) with (5.1) taken into account, we obtain:

$$\nabla \times (\varepsilon^{-1}(r)(\nabla \times \mathbf{H})) = -\frac{\mu}{c^2} \frac{\partial^2}{\partial t^2} \mathbf{H}. \quad (5.3)$$

Hence, for monochromatic waves, we have:

$$\frac{\partial^2}{\partial t^2} \mathbf{H}(r, t) = -w^2 \mathbf{H}(r, t). \quad (5.4)$$

In view of (5.4) instead of (5.3) with  $\mu = 1$  can be written:

$$\nabla \times (\varepsilon^{-1}(r)(\nabla \times \mathbf{H})) = \left(\frac{w}{c}\right)^2 \mathbf{H}. \quad (5.5)$$

Since the value of  $\varepsilon(r)$  in this case is real, then equation (5.5) is the task of finding the eigenvalues  $\omega^2/c^2$  of a Hermitian operator  $L = \nabla \times (\varepsilon^{-1}(r)\nabla \times)$  in the equation

$$L\mathbf{H} = \left(\frac{w}{c}\right)^2 \mathbf{H}. \quad (5.6)$$

Consider the one-dimensional structure of the PC with a period  $d = a + b$ , where  $a$  and  $b$  are the sizes of sites of the dielectric constants  $\varepsilon_1$  and  $\varepsilon_2$ , respectively. It is known [1, 3] that the eigenfunctions of equation (5.6) in a periodic medium have the Bloch form:

$$\varphi = e^{ikx} u(x), \quad (5.7)$$

where  $x$  is the coordinate,  $k = 2\pi/\lambda$  is the wave number. Eigenfunctions of the operator  $L$  are determined on the basis of their form (5.7) and boundary conditions defined by the function

$$\varepsilon(x) = \begin{cases} \varepsilon_1, & nd \leq x < a + nd, \\ \varepsilon_2, & a + nd \leq x < (n+1)d, \end{cases} \quad (5.8)$$

where  $n$  is an integer. The eigenfunctions in the regions with dielectric constants  $\varepsilon_1$  and  $\varepsilon_2$  will be, respectively, form

$$\begin{aligned} \varphi_1(x) &= Ae^{ik_1x} + Be^{-ik_1x}, \\ \varphi_2(x) &= Ce^{ik_2x} + De^{-ik_2x}, \end{aligned} \quad (5.9)$$

where  $A, B, C, D$  are unknown coefficients.

Since at the boundaries of zones with different dielectric constants there must be continuous both the eigenfunctions and their derivatives, we can form a system of equations:

$$\begin{cases} A + B = e^{-iQd} (Ce^{ik_2d} + De^{-ik_2d}), \\ k_2(A - B) = k_2e^{-iQd} (Ce^{ik_2d} - De^{-ik_2d}), \\ Ae^{ik_1a} + Be^{-ik_1a} = Ae^{ik_2a} + Be^{-ik_2a}, \\ k_1(Ae^{ik_1a} - Be^{-ik_1a}) = k_2(Ae^{ik_2a} - Be^{-ik_2a}). \end{cases} \quad (5.10)$$

In the matrix form, this system of equations for  $A, B, C$  and  $D$  can be written as:

$$M(k_1, k_2, Q)V = 0, \quad (5.11)$$

where

$$M(k_1, k_2, Q) = \begin{pmatrix} 1 & 1 & -e^{id(k_2-Q)} & -e^{-id(k_2+Q)} \\ k_1 & -k_1 & -k_2e^{id(k_2-Q)} & k_2e^{-id(k_2+Q)} \\ e^{ik_1a} & e^{-ik_1a} & -e^{ik_2a} & -e^{-ik_2a} \\ k_1e^{ik_1a} & -k_1e^{-ik_1a} & -k_2e^{ik_2a} & k_2e^{-ik_2a} \end{pmatrix}, \quad (5.12)$$

$$V = \begin{pmatrix} A \\ B \\ C \\ D \end{pmatrix}.$$

This system of equations has a nontrivial solution if  $\det M = 0$ . Expanding the determinant we can obtain in an implicit form the dispersion relation  $\omega(Q)$ :

$$\cos(k_1a)\cos(k_2b) - \frac{1}{2} \frac{\varepsilon_1 + \varepsilon_2}{\sqrt{\varepsilon_1\varepsilon_2}} \sin(k_1a)\sin(k_2b) = \cos(Qd), \quad (5.13)$$

where  $k_i = \sqrt{\varepsilon_i} \frac{\omega}{c}$ ,  $i = 1, 2$ ,  $Q$  is the Bloch wave number. Since  $|\cos(Qd)| \leq 1$ , band gaps form in the spectrum, i.e. the values of  $k_i$  for which

$$\left| \cos(k_1a)\cos(k_2b) - \frac{1}{2} \frac{\varepsilon_1 + \varepsilon_2}{\sqrt{\varepsilon_1\varepsilon_2}} \sin(k_1a)\sin(k_2b) \right| > 1. \quad (5.14)$$

In these areas, the propagation of radiation in a crystal is impossible. Or conversely, given a one-dimensional photonic crystal ( $a, b, \varepsilon_1, \varepsilon_2$ ), from the inequality (5.14) we find  $\omega = 2\pi\nu$  – the cyclic frequency of light that can pass through a photonic crystal.

Consider the simplest one-dimensional theory. We can now consider some examples of the model. Consider the diffraction of a plane wave on photonic crystals in two dimensions. In all the examples in this section, a wave of unit intensity ( $E_0 = 1$  V/m). Modelling was performed using the program FullWAVE 6.0 and the FDTD method implemented in it.

### ***5.1.2. Plane wave diffraction on photonic crystals without defects***

Consider the incidence of a plane electromagnetic wave c TE-polarization on a photonic crystal (PC). PC parameters are taken from [4] to obtain comparable results:  $n_1 = 3.25$  – refractive index of the medium,  $n_2$  – refractive index of a hole,  $r = 0.25 \mu\text{m}$  – the radius of the holes,  $T_z = 0.6 \mu\text{m}$  and  $T_x = 1 \mu\text{m}$  – distance between the centres of the holes on the optical axis  $z$  and  $x$ , respectively. The fill factor on the axis  $z$ :  $\Lambda_z = 0.83$ , on the axis  $x$ :  $\Lambda_x = 0.5$ , also taken from [4]. Figure 5.1 shows the band gap for a given crystal for TE-polarization. The length of the electromagnetic wave  $\lambda = 1.55 \mu\text{m}$ . Figure 5.1 shows that this wavelength lies in the photonic band gap, the reflection coefficient  $R \approx 0.89$ . Figure 5.2 shows that the light of this wavelength does not enter the crystal further the first three layers of holes. Now consider the same photonic crystal, but change the wavelength at  $\lambda = 2.2 \mu\text{m}$ . Figure 5.3 shows that at this wavelength PC transmits electromagnetic radiation, the reflection coefficient is small,  $R \approx 0.2$ .

That is, the band gap in Fig.5.1 is not an exact function-rectangle (rect) and the light reflection coefficient reaches the maximum value of 1 in connection with the fact that the simulation considers the finite size of PC on the coordinates  $x$  and  $z$ .

### ***5.1.3. Propagation of light in a photonic crystal waveguide***

Consider the same photonic crystal as in the preceding paragraph by removing the three central rows of holes. The wavelength is chosen on the basis of Fig. 5.1 so that the transmission coefficient was minimal.

This condition is satisfied for  $\lambda = 1.55 \mu\text{m}$ . Figure 5.4 shows the light propagation in a photonic crystal waveguide. Figure 5.4 shows that light travels only in the way that we created in a photonic crystal by removing three adjacent rows of holes.

Now let us reduce the radiation source to the dimensions of the waveguide in order to assess the power loss when light passes through a waveguide (Fig. 5.5). The energy loss at a distance of  $5 \mu\text{m}$  (the length of the waveguide) was approximately 0.51%. That is, if we focus the light at the entrance of the photonic-crystal waveguide about  $1 \mu\text{m}$  wide, the light passes almost completely through it to the exit.

### ***5.1.4. Photonic crystal collimators***

Optimization methods [5] for the structure of photonic crystal waveguides to reduce the beam divergence at the exit of the fibre have recently been developed. For conventional optical fibres this problem is solved by means of structuring the output of the fibre tip.

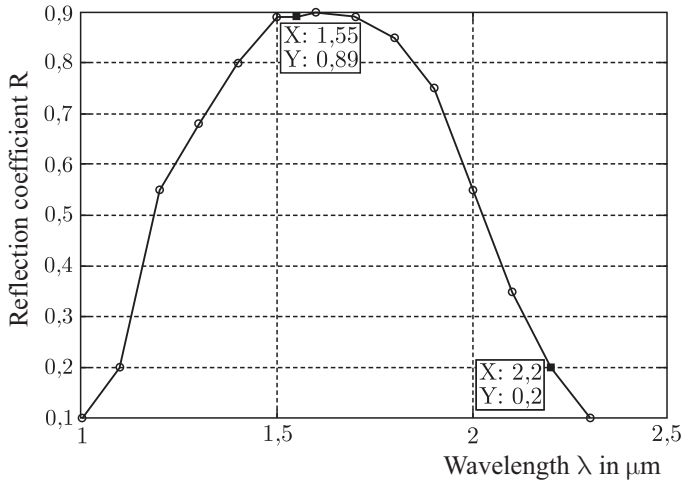


Fig. 5.1. Photonic forbidden band.

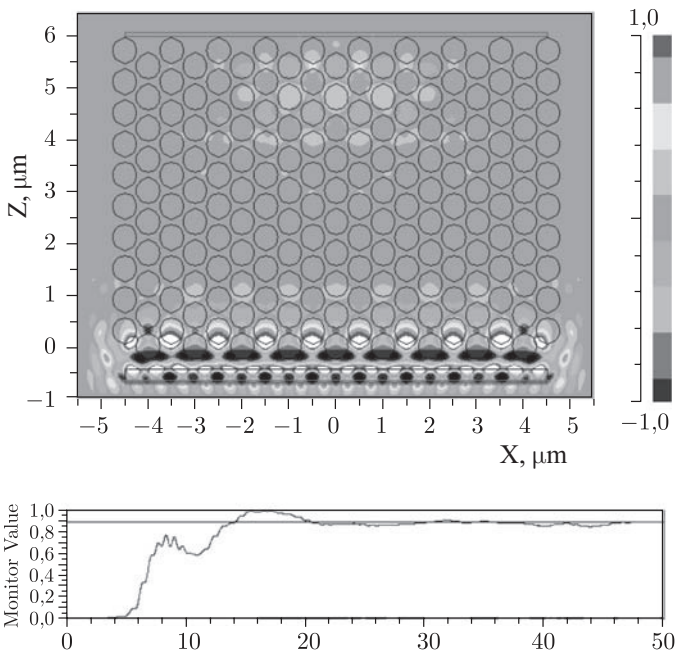
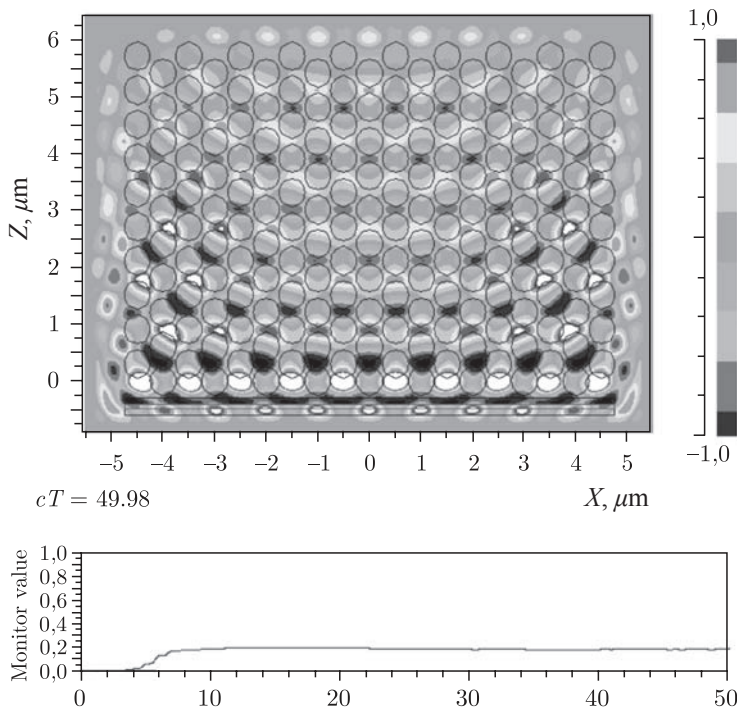
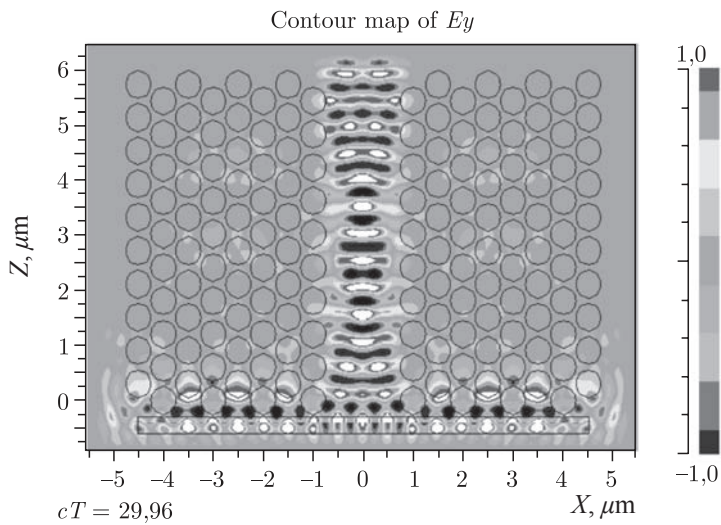


Fig. 5.2. Propagation of light in a photonic crystal in the band gap. Light travels from the bottom up.

Figure 5.6a shows a schematic of a two-dimensional photonic crystal waveguide, the shell of which consists of periodically spaced (period 228 nm) dielectric nanorods ( $\epsilon = 3.38$ , silicon) of 114 nm. To create a waveguide a row of nanorods is



**Fig.5.3.** Light propagation in a photonic crystal outside the band gap. Light travels from the bottom up.



**Fig. 5.4.** Propagation of light in a photonic crystal waveguide.

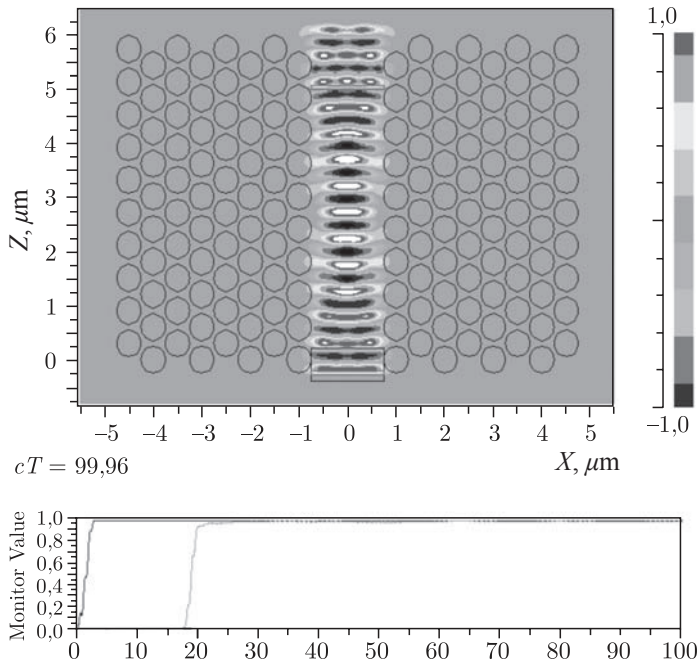


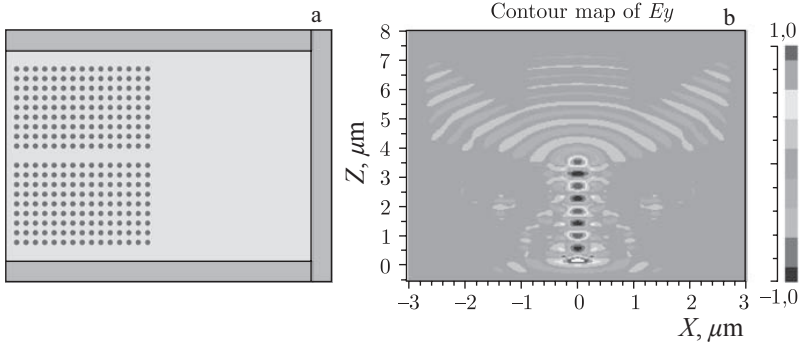
**Fig. 5.5.** Propagation of light in a photonic crystal waveguide with a narrow light source. Light travels from the bottom up.

removed. The size of this ‘defect’ in the periodic structure of the nanorods is 342 nm and a half period. The light wavelength 633 nm. Figure 5.6b shows an instantaneous picture of the diffraction of light on this structure, calculated by the FDTD method with FullWAVE programme. We see that the light does not go into the shell and propagates inside the waveguide side with a refractive index of 1. At the exit from the waveguide the light wave is strongly divergent, extending at an angle of 140°.

Note that the width of the waveguide (342 nm) is slightly more than half the length of light (633 nm). Some modernization of the structure of the waveguide near the exit can greatly reduce the beam divergence. Thus, Fig. 5.7a shows the PC-waveguide in which two rods in the back row near the waveguide side were removed. This led to the situation in which the radiation after the waveguide diverges at an angle of only 30° (Fig. 5.7b). Note that in the scalar theory of diffraction the full angle of divergence can be estimated as  $2\lambda/\pi r = 2.35$ , or 130°,  $r$  is the radius of the waveguide side.

## 5.2. Two-dimensional photonic crystal gradient Michaelian lens

Modern technology allows manufacture of the optical micro- and nano-objects with dimensions comparable to the wavelength of light. So the question arises of computer simulation of light diffraction on such objects. To solve this problem, we must solve directly Maxwell’s equations. One of the most widely used methods for the



In **Fig. 5.6** Photonic-crystal waveguide (a) and diffraction pattern of light inside the waveguide and exit (b). Light travels from left to right.

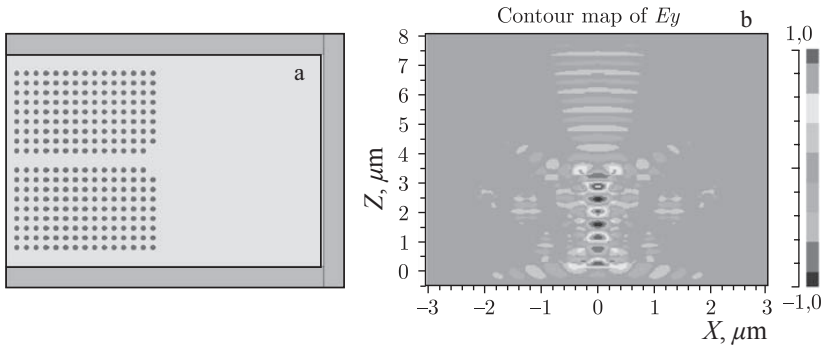


**Fig. 5.7.** Photonic-crystal waveguide with a collimator (a) and diffraction pattern of light inside the waveguide and at the exit from it (b). Light travels from left to right.

numerical solution of these equations is the ‘finite-difference time-domain method’ (FDTD) [6]. This method worked well, thanks to its versatility in solving diffraction problems [7, 8]. It is used in this section.

Photonic crystals, which we briefly discussed in the previous section, are structure with a periodically varying refractive index (this period should be smaller than the wavelength), which allow the manipulation of light at the nanometer scale [9]. Recently, they have attracted increasing attention due to a number of their interesting properties. One of the fundamental properties of these materials is that they do not reflect light at certain wavelengths. This spectral region is called a ‘photonic band gap’. Currently, the most interesting are photonic crystals in which the band gap lies in the visible or near infrared regions [10–13].

Through the development of production technology of photonic crystals it is possible to create a photonic crystal lens. The PC lens is a photonic crystal in which the radius of the hole changes according to a specific law, which ensures focusing of light. The period of the crystal lattice remains constant. These lenses, for example, solve the problem of focusing light on the input of the photonic crystal waveguide, being a more compact alternative to microlens and tapered waveguides.

It is known that the gradient medium with the radial dependence of the refractive index in the form of a  $\text{sech}^2$  hyperbolic secant, proposed in [14], is used for self-focusing of laser radiation. The gradient lens with such refractive index collects all the rays parallel to the axis in the focus on the surface and is called the Michaelian lens. In [15] it is proposed to search for the mode solution of the wave equation for the 2D gradient medium with the refractive index in the form of a  $\text{sech}^2$  hyperbolic secant, similar to finding soliton solutions of the non-linear Schrödinger equation.

This section describes the paraxial and non-paraxial solutions in the form of a  $\text{sech}^2$  hyperbolic secant for two-dimensional gradient waveguide whose refractive index depends on the transverse coordinate in the form of a  $\text{sech}^2$  hyperbolic secant. For a cylindrical gradient lens we find a similar photonic crystal lens which can be produced by photo- or electronic lithography. The FDTD method implemented in the programming language C++ is used for comparative simulation of a plane wave passing through both microlens.

### 5.2.1. The modal solution for the gradient $\text{sech}^2$ environment

In 1951, A.L. Mikaelian showed [14] that in the gradient medium with cylindrical symmetry and the dependence of the refractive index on the radial coordinate as a function of the  $\text{sech}^2$  hyperbolic secant all the rays, emanating from the same axial point, at some distance again gather in the axial focus. This phenomenon is called self-focusing of light in a gradient medium.

It can be shown that a two-dimensional gradient medium, whose refractive index depends on the transverse coordinates in the form of the function of the hyperbolic  $\text{sech}^2$  is characterized by spreading of the light field, which retains its structure, showing modal (soliton) properties, and its complex amplitude is proportional to the same function of the hyperbolic secant.

Indeed, suppose that the distribution of the refractive index in the 2D model of the gradient medium depends only on the transverse coordinates in the form of the function of the hyperbolic  $\text{sech}^2$ :

$$n(y) = n_0 \text{sech}^2 \left( \frac{kn_0 y}{\sqrt{2}} \right), \quad (5.15)$$

where  $n_0$  is the maximum refractive index of the medium on the optical axis,  $k$  is the wave number of light in vacuum. In the case of TE-polarization the only non-zero projection of the vector of the strength of the electric field of a monochromatic electromagnetic wave  $E_x(y, z)$  satisfies the Helmholtz equation:

$$\left[ \frac{\partial^2}{\partial z^2} + \frac{\partial^2}{\partial y^2} + \frac{k^2 n_0^2}{ch^2 \left( \frac{kn_0 y}{\sqrt{2}} \right)} \right] E_x(y, z) = 0, \quad (5.16)$$

where  $z$  is the direction along the optical axis. Then the modal solution of (5.16) in

the form of a ‘soliton’ will look like:

$$E_x(y, z) = E_0 \operatorname{ch}^{-1} \left( \frac{kn_0 y}{\sqrt{2}} \right) \exp \left( \frac{ikn_0 z}{\sqrt{2}} \right), \quad (5.17)$$

where  $E_0$  is a constant. The word ‘soliton’ is in quotes, as in our case there is no non-linearity, and the solution (5.17) just looks like a soliton solution and is made of the given gradient medium. Interestingly, the solution (5.17) holds in the paraxial case. If instead of the gradient medium (5.15) we choose a somewhat different dependence of the refractive index on the transverse coordinates:

$$n_1(y) = n_0 \sqrt{1 + \operatorname{ch}^{-2} \left( \frac{kn_0 y}{\sqrt{2}} \right)}, \quad (5.18)$$

where  $n_1(0) = \sqrt{2}n_0$  is the maximum refractive index, and  $n_1(\infty) = n_0$  is the minimum refraction index, the solution of the paraxial equation

$$\left[ 2ik \frac{\partial}{\partial z} + \frac{\partial^2}{\partial y^2} + \frac{k^2 n_0^2}{\operatorname{ch}^2 \left( kn_0 y / \sqrt{2} \right)} \right] E_{1x}(y, z) = 0, \quad (5.19)$$

will be similar to the complex amplitude (5.17):

$$E_{1x}(y, z) = E_0 \operatorname{ch}^{-1} \left( \frac{kn_0 y}{\sqrt{2}} \right) \exp \left( \frac{ikn_0^2 z}{4} \right). \quad (5.20)$$

Note that the solutions (5.17) and (5.20) have finite energy:

$$W = \int_{-\infty}^{\infty} |E_x(y, z)|^2 dy = |E_0|^2 \int_{-\infty}^{\infty} \operatorname{ch}^{-2} \left( kn_0 y / \sqrt{2} \right) dy = 2 |E_0|^2. \quad (5.21)$$

Modal solutions, similar to (5.17) and (5.20), can be found for the 3D gradient waveguide with a refractive index:

$$n(x, y) = n_0 \operatorname{ch}^{-1} \left( bx + y \sqrt{\frac{(kn_0)^2}{2} - b^2} \right), \quad (5.22)$$

where  $b$  is an arbitrary parameter. A method of producing such a  $\operatorname{ch}^{-1}$  solutions can be found in recent papers of I.V. Alimenkov [16,17] in which 3D-soliton solutions were found for non-linear Schrödinger equation with the Kerr non-linearity of the third order, when the refractive index of the non-linear medium is described by:

$$n^2(x, y, z) = n_0^2 + \alpha I(x, y, z), \quad (5.23)$$

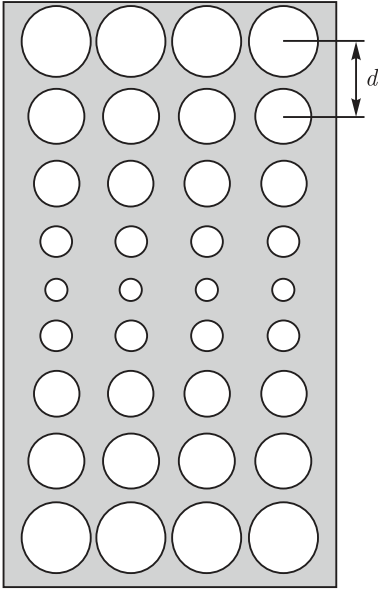


**Fig. 5.8.** Photonic crystal gradient lens.

where  $a$  is a constant,  $I(x, y, z) = |E(x, y, z)|^2$  is the intensity of one of the components of the electric field vector of the light wave. The analogy between the soliton ch<sup>-1</sup> solution of the non-linear medium (5.23) and a linear gradient medium with a refractive index (5.15) or (5.18) was first pointed out by A.W. Snyder [15].

The next section shows how to replace the cylindrical gradient lens (GL) by a 2D photonic crystal lens.

### 5.2.2. Photonic crystal gradient lens

A two-dimensional photonic crystal gradient lens (PCGL) consists of a photonic crystal in which the radius of holes varies according to a definite law. Like a conventional lens, PCGL can focus a parallel light beam to a point. However, PCGL can be more compact and can be easier to manufacture. Figure 5.8 shows schematically the PCGL.

The cylindrical ??? GL [14] is a gradient lens, whose refractive index varies from centre to edge of the lens according to the law:

$$n(y) = \frac{n_0}{\text{ch}\left(\frac{\pi|y|}{2L}\right)}, \quad (5.24)$$

where  $L$  is the width of the lens along the axis  $z$ ,  $n_0$  is the refractive index in the centre.

We choose the equivalent PCGL from a material with a refractive index  $n$  and thickness along the optical axis  $a$  so that it could be replaced by the GL. For this we require that at discrete points of this lens the optical path length is equal to the optical path length in the GL. The optical path length in the GL will be:

$$\Delta_1 = \frac{Ln_0}{\text{ch}\left(\frac{\pi|y|}{2L}\right)}. \quad (5.25)$$

The optical path length in the PCGL is:

$$\Delta_2 = N[2r(y) + (d - 2r(y))n], \quad (5.26)$$

where  $N$  is the number of holes in a row,  $d$  is a constant of the crystal or the distance between the centres of holes,  $r(y)$  is the radius of holes, varying from row to row. Equating the optical lengths (5.25) and (5.26), we obtain the following expression for the radius

$$r(y) = \frac{d}{2(n-1)} \left( n - n_0 \frac{1}{\text{ch}\left(\frac{\pi|y|}{2L}\right)} \frac{L}{a} \right). \quad (5.27)$$

Suppose that in each column of the lens there are  $M$  holes. Then the obtained dependence should be performed at the points  $y = \pm dm$  and  $m$  varies from 0 to  $M/2$ . In this case the radius of the hole should also be subjected to certain conditions. First, the radius must be non-negative. It follows from (5.27) that the minimum radius is attained at  $y = 0$ . Applying a non-negativity condition to it, we obtain the following relation for the parameters of the GL and the corresponding PCGL:

$$na \geq n_0L. \quad (5.28)$$

Secondly, the diameter of the hole obviously must be less than the constant of the crystal. The maximum radius is attained at  $y = b/2$ , where  $b$  is the aperture of the lens. The above condition imposes the following restriction on the aperture of the lens:

$$\text{ch}\frac{\pi b}{4L} < n_0 \frac{L}{a}. \quad (5.29)$$

Third, the period of the lattice, as mentioned above, should be subject to the condition  $d < \lambda$ . In addition, in the numerical simulation of the photonic crystal lens the grid step??? should be chosen so small that the radius varies from row to row. The fact is that it may happen that the change in radius from row to row may be less than the sampling step. In this case, the radius does not change and the desired effect would not be reached.

Simulation of light diffraction on 2D micro-lenses was performed using a finite difference solution of Maxwell's equations by the FDTD-method. The C++ language in the MS Visual Studio 6.0 was used to implement the Yee algorithm [18] in the two-dimensional case for TE-polarization. Input of radiation in the computational domain is implemented using the 'total field-scattered field' condition [19]. The boundary conditions are represented by perfectly absorbing Berenger layers (J.P. Berenger) [20].

GL has the property of focusing light to a point on the surface. In our numerical experiments we used the GL with the following parameters: wavelength  $\lambda = 1.5 \mu\text{m}$ ,  $L = 3 \mu\text{m}$ ,  $n_0 = 1.5$ ,  $b = 4 \mu\text{m}$ . The distribution of the squared modulus of the complex amplitude of the electric field when light passes through such a lens is shown in Fig. 5.9, and the cross section of intensity in Fig. 5.10.

The graph shows that the focus of such a lens is exactly the same as its front surface.

We now simulate the passage of light through PCGL with parameters  $a = L = 3.4 \mu\text{m}$ ,  $n = n_0 = 1.5$ ,  $d = 0.254 \mu\text{m}$ . Figure 5.11 shows the dependence of the radius of holes (Fig. 5.8) in the FLM on the number of some of these holes.

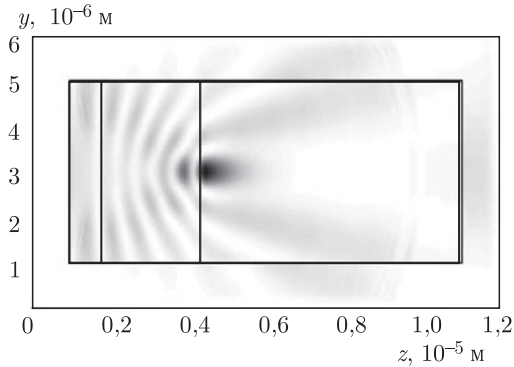


**Fig. 5.9.** The distribution of the squared modulus of the electric field  $|E_x|^2$  (negative) of the GL, the location of the lens is indicated by a gray rectangle.

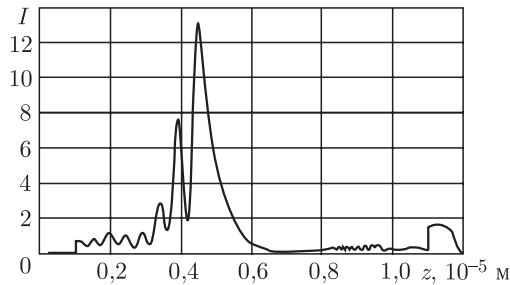


**Fig. 5.10.** The distribution of the squared modulus of the electric field in the cross section along the main axis of the GL.

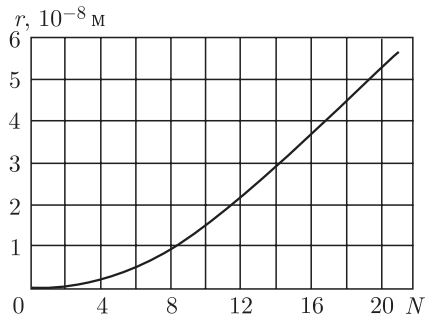


**Fig. 5.11.** Dependence of the radius of the holes on the number of the row.

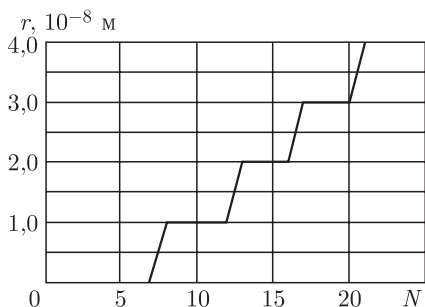


**Fig. 5.12.** Dependence of the radius of the holes on the number of rows in the sample of 100 samples per wavelength.

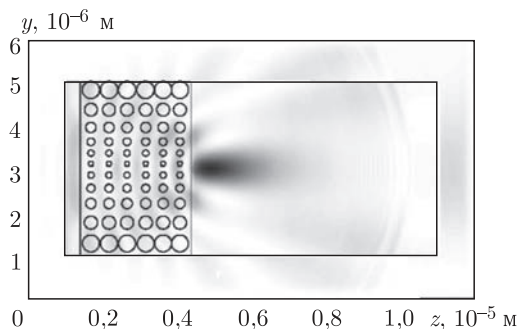


**Fig. 5.13.** The distribution of the squared modulus of the electric field  $|E_x|^2$  (negative) in PCGL.

However, even with large sample  $\lambda/h = 100$ , it turns out to be quite an inaccurate approximation of the radius. This is shown in Fig. 5.12.

The period of the nanostructure of the holes is 250 nm, the minimum hole diameter 10 nm, maximum 40 nm. Figures 5.13 and 5.14 show the distribution of the squared modulus of the complex amplitude of light passing through the lens.

We see that the focus of this lens is at a distance of  $f = 3.3 \mu\text{m}$  from the beginning of the lens, i.e. accurately corresponds to the GL with  $L = 3 (\mu\text{m})$ . The intensity in the focus is  $I_f = 7.5$ , which is less than in the GL (PCGL efficiency is 70% of the efficiency of GL), and the focal length of the PCGL on the  $z$ -axis twice that of the

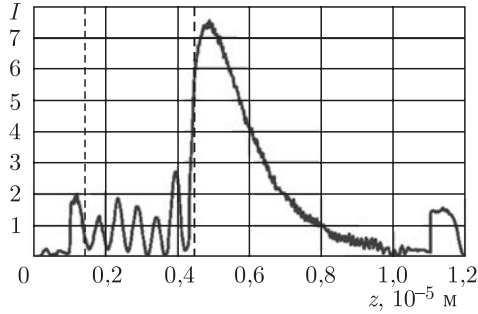


**Fig. 5.14.** The distribution of the squared modulus of the electric field along the main optical axis PCGL.

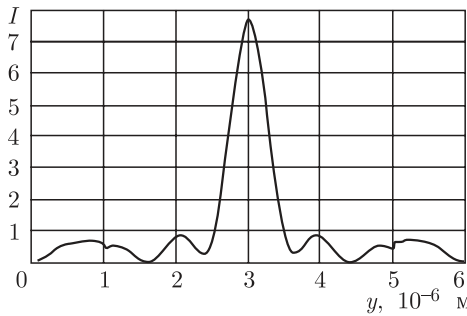


**Fig. 5.15.** The distribution of the squared modulus of the electric field in the focal plane

GL. This is due to the small sampling and rough approximation (Fig. 5.12) of the curve in Fig. 5.11. Figure 5.14 shows ‘noise’ caused by the coupling terms of ‘the total field–scattered field’ procedure (this is not the physical noise). The distribution of the squared modulus of the electric field in the focal plane is shown in Fig. 5.15.

Figure 5.15 shows that the diameter of the focal spot of the PCGL according to the half-time of intensity is equal to  $\text{FWHM} = 0.42\lambda$ . FWHM is the abbreviation of full width half maximum. Note that in the scalar case for the focal spot, the intensity of which is described by the sinc-function, it is known that the width of the focal spot according to the half-time is  $0.44\lambda/\text{NA}$ , where NA is the numerical aperture of the lens. In the case of PCGL  $\text{NA} = 0.67$ , so the width of the spots according to the half-time is equal to  $0.29\lambda/\text{NA}$ . This is 1.5 times less than in the scalar case.

### 5.2.3. The photonic crystal lens for coupling two waveguides

In recent years, various micro-and nanophotonic devices have been actively investigated for coupling two waveguides of different types, for example, a conventional single-mode fibre with a wire or a planar waveguide or a planar waveguide with a photonic crystal (PC) waveguide. The following nanophotonic device are available for pairing of two waveguide structures: an adiabatically

tapered ridge waveguides for coupling with the PC-waveguides [21–27]; waveguide structures can not only dock with each other by output to input, but can also overlap parallel to each other [28], Bragg gratings in a waveguide [29–32] to extract the radiation from the fibre, the fibre with the Bragg grating can be placed on the surface of a planar waveguide [33], a parabolic micromirror at an angle to enter into a planar waveguide [34], conventional refractive lenses or microlenses [35–38], Veselago superlens with negative refraction: plane [39–46] or with a concave surface [47–49], the interface in the millimeter range: superlens [50, 51] and PC-lens [52]. Work is also being carried out to combine two different PC waveguides [53].

Tapered waveguides can be highly effective communication devices if the widths of the mode in the ridge waveguide and in the PC-waveguide are comparable with each other. In this case, the effectiveness of communication (i.e. the ratio of the energy at the output of the device to the energy at the input) can reach 80% [21], 90% [24], 95% [22], and even nearly 100% [26]. If the width of the ridge waveguide ( $1.6 \mu\text{m}$ ) is several times larger than the width of PC-waveguide (200 nm), the effectiveness of communication is reduced to 60% [23]. At an even greater difference in the widths of the mating waveguides the size of the adiabatically narrowing (tapered) waveguide is relatively large: in the compression of the mode of the single-waveguide fibre with the core diameter of  $4.9 \mu\text{m}$  to the size of the mode of a planar waveguide with a width of 120 nm, the length of the taper is  $40 \mu\text{m}$  [25], and the waveguide with a cross section of  $0.3 \times 0.5 \mu\text{m}$  narrows to 75 nm in diameter at a distance of  $150 \mu\text{m}$  [27].

Coupling devices, which transfer radiation from a single-mode fibre to planar waveguides or photonic-crystal waveguides with the grating on the waveguide also have tapered areas. For example, the tapering of a Gaussian beam with a waist diameter of  $14 \mu\text{m}$  to the size of the waveguide with a width of  $1 \mu\text{m}$  is carried out using a taper only  $14 \mu\text{m}$  long [29, 30]. In this regard, the experimental efficiency of coupling is 35% [10], without a mirror layer on the reverse side of the waveguide, and 57% [29] with a mirror. Input of the Gaussian beam with a wavelength of  $1.3 \mu\text{m}$  into the waveguide was performed with a diffraction grating on the waveguide [30]. A similar device is connected to the grating on a silicon waveguide with a period of 630 nm and a 20–40  $\mu\text{m}$  taper, but for a wavelength of  $1.55 \mu\text{m}$  the experimental efficiency was 33% (with a mirror 54%) [31]. Higher quality has an input device for transferring radiation from a single-mode fibre with a diffraction grating in silicon with a period of 610 nm and a width of  $10 \mu\text{m}$  to a wire waveguide 3  $\mu\text{m}$  wide with an experimental communication efficiency of 69% [32]. The computed communication efficiency over 90% has the J-coupler, which connects a wide waveguide ( $10 \mu\text{m}$ ) with an PC-waveguide (420 nm) using a parabolic mirror with the size of  $15 \times 20 \mu\text{m}$  for a wavelength of  $1.3 \mu\text{m}$  [34]. In this case both the waveguide and the parabolic mirror are made of a silicon film (refractive index  $n = 3.47$ ).

Conventional refractive lenses and microlenses have also been successfully applied in coupling problems. For example, a silicon waveguide ( $n = 3.092$ ) 1–2  $\mu\text{m}$  wide has a lens at the end which allows this waveguide to be coupled with a silicon PC-waveguide ( $n = 3.342$ ) with a calculated 90% efficiency [35]. Modelling has shown [37] that the single-mode fibre with a diameter  $3.10 \mu\text{m}$  (wavelength

$\lambda = 1.55 \mu\text{m}$ ) with a collimating lens of VK7 glass (numerical aperture  $\text{NA} = 0.1$ ) with radius  $R = 1.77 \text{ mm}$  and with a focusing silicon microlens with a radius of  $123 \mu\text{m}$  can be coupled with a PC-waveguide with a cross section of the mode of  $0.19 \times 0.27 \mu\text{m}$  with an efficiency of 80%. At the same time the microlens creates inside the PC-waveguide a focal spot with a diameter ???  $\text{FWHM} = 0.24\lambda$  (numerical aperture of the waveguide  $\text{NA} = 2.2$ ).

A special place among the couplers is occupied by the devices based on 2D superlenses (or Veselago lens), which are based on the phenomenon of negative refraction. A superlens with an effective refractive index close to  $-1$  can be produced using photonic crystals. The superlens is used to image a point source. The first image appears inside the lens and the second image behind the lens at a distance of  $2B - A$ , where  $B$  is the thickness of plane-parallel lenses,  $A$  is the distance from the lens to the source [39, 43]. In [41] it is shown that if a 2D point light source is described by the Hankel functions  $H_0(kr)$ ,  $k$  is the wave number,  $r$  is the distance from the source to the observation point, then the image will be proportional to the Bessel function  $J_0(kr)$ . That is the spot image formed by the superlens has a diameter  $\text{FWHM} = 0.35\lambda$ . In [44] simulation of the 2D photonic-crystal superlens have shown that if the lens consists of two layers of dielectric rods (dielectric constant  $\varepsilon = 12.96$ ) for the wavelength  $\lambda = 1.55 \mu\text{m}$  with the radius  $r = 0.45a$ , where  $a$  is the period of the grating rods, then at the cyclic frequency  $\omega = 0.293a/\lambda$  the refractive index is equal to  $n = -1$ , and a point source located at a distance  $A = 0.26\lambda$  from the lens is imaged at approximately the same distance on the other side of the lens, and the width of the image spot is  $\text{FWHM} = 0.36\lambda$ . In some studies attention was paid to Veselago lenses not in the form of a plane-parallel PC layer but with one surface being concave. For example, in [47] it was shown that PC-lens of a rectangular grating of rods with  $\varepsilon = 10$  and the magnetic permeability  $\mu = 1.5$  with a period of  $a = 0.48 \text{ cm}$ , the radius of ???  $r = 0.4a$ , has an effective refractive index of  $n = -0.634$ . Also, if this 2D lens is plane-concave with a radius of curvature  $R = 3.31 \text{ cm}$ , the focus of such a superlens would be located at a distance  $f = R/(1-n)$ , for TE-polarization  $f = 1.69 \text{ cm}$ , while for TM-polarization,  $f = 2.38 \text{ cm}$ . The radiation frequency is equal to  $\omega = 0.48a/\lambda$ . In [48], the results are presented of modelling of the input of radiation in a PC-waveguide with a superlens with a concave surface. The PC-lens had a thickness of  $8.6a$  and an aperture of  $38a$ , while the PC consisted of a 2D grating of holes with a period  $a = 465 \text{ nm}$  in GaAs ( $\varepsilon = 12.96$ ) and a diameter  $2r = 372 \text{ nm}$ . In the focus of the lens at a distance of  $7.56\lambda$  ( $\lambda = 1.55 \mu\text{m}$ ) there formed a focal spot with a radius of radius  $0.5\lambda$ , if the lens was illuminated with a Gaussian beam with a waist radius of  $3\lambda$ . Then radiation behind the lens travelled to the 3W PC-waveguide (3W means that the width of the waveguide is equal to three grating periods of the PC) with a width of  $3a$  (approximately  $\lambda$ ). Unfortunately, the efficiency of input to such a structure was not given in [48]. In [49] the authors also discussed the results of modelling the input of radiation from a single-mode fibre to a PC waveguide with FC-superlens (plano-concave,  $n = -1$ ). The thickness of the lens was  $16a = 4.8\lambda$ , aperture  $25a$ , and it consisted of a triangular grating of holes with a period  $a = 0.305\lambda$  and radius  $r = 0.4a$  in GaAs. The radius of curvature of the concave lens surface was  $R = 2.1\lambda$ , the focal length  $f = 1.05\lambda$ .

The effective input in the PC-waveguide with  $\varepsilon = 12.96$ ,  $r' = 0.2a$ ,  $a' = 0.312\lambda$  was equal to 95%. The width of the waveguide is equal to one period of photonic-crystal lattice  $a$ , and angular frequency  $\omega = 0.315a/\lambda$ . Unfortunately, the size of the focal spot of this lens was not given.

A different type of PC lens was studied in [54–56]. The grating of holes in such 2D PC lens has a constant period, but the size of the holes is changed according to some function. In the Mikaelian gradient lens [14] all rays parallel to the optical axis and falling perpendicular to its flat surface are collected in a point on the optical axis on the opposite flat surface. Such an axially-symmetric lens has the dependence of the refractive index on the radial coordinate (distance from the optical axis) in the form (6.24). In [43] the authors simulated a 2D Michaelian lens with an aperture of  $12\ \mu\text{m}$ , consisting of 7 columns of holes with a period of  $0.81\ \mu\text{m}$  for the wavelength  $\lambda = 1.55\ \mu\text{m}$ . The efficiency of input from a wide waveguide ( $12\ \mu\text{m}$ ) into the PC-waveguide  $1.5\ \mu\text{m}$  wide with the effective refractive index  $n = 1.73$  was 55%. The PC-waveguide consists of a lattice of holes with a period of  $0.63\ \mu\text{m}$  and a diameter of  $0.4\ \mu\text{m}$ . In this study the characteristics of the focal spot of the lens are again not given. In [55, 56] a similar PCGL, but with different parameters was simulated. The lens thickness  $3\ \mu\text{m}$ , 12 columns of holes, aperture of the lens  $4\ \mu\text{m}$ , the refractive index of 1.5, wavelength  $1.5\ \mu\text{m}$ . The diameter of the focusing spot was FWHM  $= 0.42\lambda$ , and the focal spot diameter from zero to zero intensity was equal to  $0.8\lambda$ .

This section examines the ultracompact nanophotonics device enabling the effective coupling of 2D waveguides of different widths using PCGL. The device was manufactured by the ‘silicon on silica’ technology, the width of the input waveguide was  $4.5\ \mu\text{m}$ , the width of the output waveguide  $1\ \mu\text{m}$ , the size of the PCGL  $3\times 4\ \mu\text{m}$ . The lens consisted of a matrix of holes  $12\times 17$  with the period of the lattice of holes  $250\ \text{nm}$ , and the diameter of the holes varied from centre to the periphery from  $160$  to  $200\ \text{nm}$ . The device operates in the wavelength range  $1.5$ – $1.6\ \mu\text{m}$ . The calculated efficiency of communication ranged from 40% to 80%, depending on the width of the output waveguide. PCGL focuses light into a small focal spot in the air just behind the lens, which ??? decay of intensity??? is equal to FWHM  $= 0.36\lambda$ , which is 1.4 times smaller than the scalar diffraction limit of resolution in the 2D case, which is determined by the width of the sinc-function and is equal to FWHM  $= 0.44\lambda$ .

### Modeling of photonic crystal waveguide lens

The photonic crystal gradient lens, which is modelled in the work, consisted of a matrix of  $12 \times 17$  holes in silicon (the effective refractive index for TE-waves is  $n = 2.83$ ), the lattice constant of holes  $250\ \text{nm}$ , the minimum diameter of the holes on the optical axis  $186\ \text{nm}$ , the maximum diameter of the holes on the edge of the lens  $250\ \text{nm}$ . The thickness of the lens along the optical axis  $3\ \mu\text{m}$ , the width of the lens (aperture)  $5\ \mu\text{m}$ . Wavelength  $\lambda = 1.55\ \mu\text{m}$ .

Modelling was performed using the difference method for solving Maxwell’s equations FDTD, implemented in the programming language C++. Figure 5.16a shows a 2D PC lens in silicon, as described above, and Fig. 5.16b shows the two-dimensional halftone diffraction pattern (averaged over time) of a plane wave of

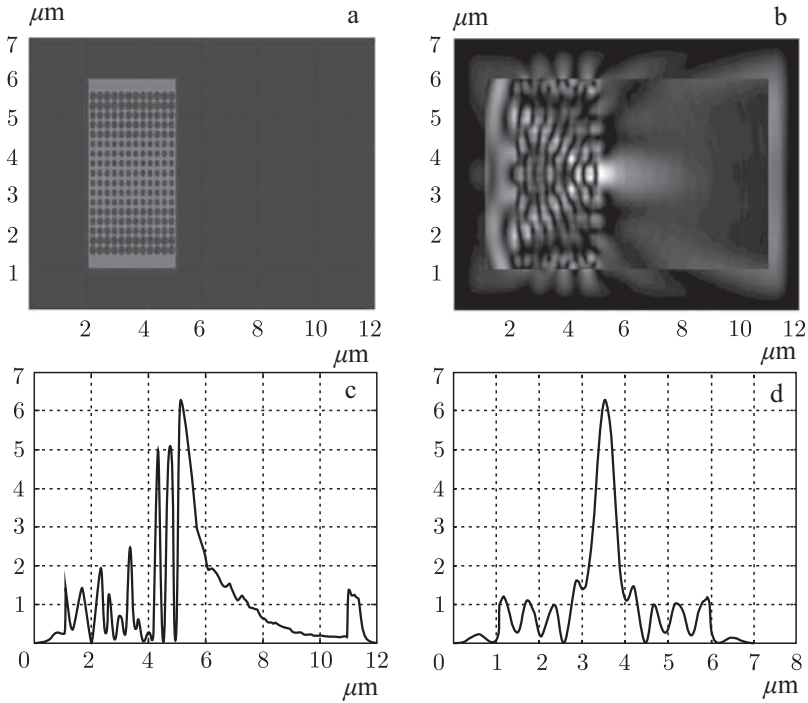


**Fig. 5.16.** 2D PCGL 12 $\times$ 17 holes in silicon, the size 3 $\times$ 4 mm (a), the field of diffraction of light (a plane TE-wave) or 2D-intensity distribution  $|E_x|^2$ ,  $y$  is the vertical axis,  $z$  is the horizontal axis (b), the intensity distribution along the optical axis (a) and in the focus plane (d).

the TE-polarization with an amplitude  $E_x$  ( $x$ -axis is perpendicular to the plane Fig. 5.16). Figure 5.16c and Fig. 5.16d show the distribution of intensity  $|E_x(x, y)|^2$  along the optical  $z$ -axis and along the line  $y$  perpendicular to the optical axis where the focus is situated. Figure 5.16c and d shows that the size of the focal spot intensity is FWHM =  $0.36\lambda$ , and the longitudinal size of the focus is FWHM =  $0.52\lambda$ .

PCGL with the parameters of the previous example (Figure 5.16a) was simulated but PCGL was located at the outlet of the waveguide in silicon 5  $\mu\text{m}$  wide and 5  $\mu\text{m}$  long (plus the length of the lens 3  $\mu\text{m}$ , total length of the waveguide with a lens along the optical axis 8  $\mu\text{m}$ ) (Fig. 5.17a).

The diffraction field (intensity  $|E_x(x, y)|^2$ ), calculated by the FDTD method and averaged over time, is shown in Fig. 5.17b (wavelength 1.45  $\mu\text{m}$ ). Figure 5.17c shows the intensity distribution along the optical axis. A comparison of Figs. 5.16c and Fig. 5.17c shows that the intensity of the focus increased, and the amplitude of modulation of the intensity inside the lenses decreased. This is due to the fact that the difference in the refractive indices between the lens and the waveguide (Fig. 5.17c) is much smaller than the difference between the lens and the air (Fig. 5.16c) and, therefore, the amplitude of the wave reflected from the interface is smaller. Figure 5.17d shows the distribution of intensity in the lens focus along a line parallel to the  $y$  axis. Figure 5.17d shows that the diameter of

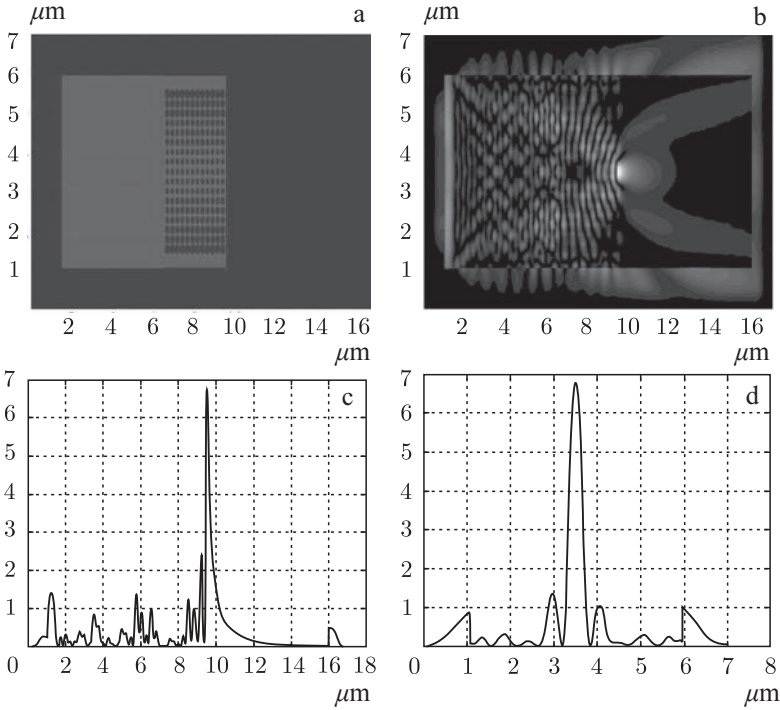


**Fig. 5.17.** 2D PCGL at the output of the waveguide (a), half-tone diffraction pattern of a plane TE-wave with amplitudes  $E_x$ , incident on the input of the waveguide  $5 \mu\text{m}$  long, the output of which contains a lens length  $3 \mu\text{m}$  long (b), the intensity distribution  $|E_x|^2$  along the optical axis (c), and the focus of the lens (d). Intensity is given in arbitrary units

the focal spot at half intensity is  $\text{FWHM} = 0.31\lambda$ . A comparison of Figs. 5.17d and Fig. 5.16d shows that in addition to decreasing diameter of the focal spot in the case of PCGL in the waveguide, the sidelobes of the diffraction pattern at the focus were also smaller.

Note that the scalar theory in the 2D case describes a diffraction-limited focus by the sinc-function:  $E_x(y, z) = \text{sinc}(2\pi y/(\lambda NA))$  which is at a maximum numerical aperture  $NA = 1$  gives the diffraction limit of the focal spot with the diameter ??? at half intensity???  $\text{FWHM} = 0.44\lambda$ . For the superlens [41], the limiting value of the focal spot is described by the Bessel function  $J_0(kr)$  and gives the value of the diameter at half intensity  $\text{FWHM} = 0.35\lambda$ . Thus, the lens in Fig. 5.17a focuses light to a spot smaller than the diffraction limit.

The simulation showed that in the wavelength range  $1.3\text{--}1.6 \mu\text{m}$  the intensity at the focus has two maximum values for the wavelengths of  $1450 \text{ nm}$  and  $1600 \text{ nm}$  (both maxima are about  $20 \text{ nm}$  wide). At other wavelengths in this range the intensity of the focus is 2–3 times smaller. With increasing wavelength the focus shifts to the lens surface, and at  $\lambda = 1.6 \mu\text{m}$  focus is inside the lens.

### Modeling of relations between the two waveguides with PCGL

Figure 5.18a shows the coupling of two 2D waveguides using PCGL. The width of the input waveguide is  $5 \mu\text{m}$ , the output waveguide  $0.5 \mu\text{m}$ . PCGL in silicon ( $n = 2.83$ ) has a matrix of  $12 \times 10$  holes with the grating period of  $0.25 \mu\text{m}$ . The diameters of the holes are the same as in previous examples. The wavelength  $1.55 \mu\text{m}$ . Both waveguides are  $6 \mu\text{m}$  long.

Modelling was performed using the FDTD method, implemented in the program FullWAVE 6.0 (the company RSoft). Figure 5.18b shows the instantaneous diffraction pattern of a TE-wave. The effectiveness of communication is 45%. Part of the radiation (20%) is reflected from the lens back into the input waveguide, another part of the radiation passes through the lens, but does not fall into a narrow waveguide. Fig. 5.18c shows an enlarged fragment of the diffraction pattern in Fig. 5.18b at the outlet of a narrow output waveguide. Unfortunately, in this program the y axis is not the transverse axis, as shown in Fig. 5.16 and Fig. 5.17, and the axis x is transverse. The intensity distribution  $|E_y(x, y)|^2$  along the transverse axis x at the outlet of

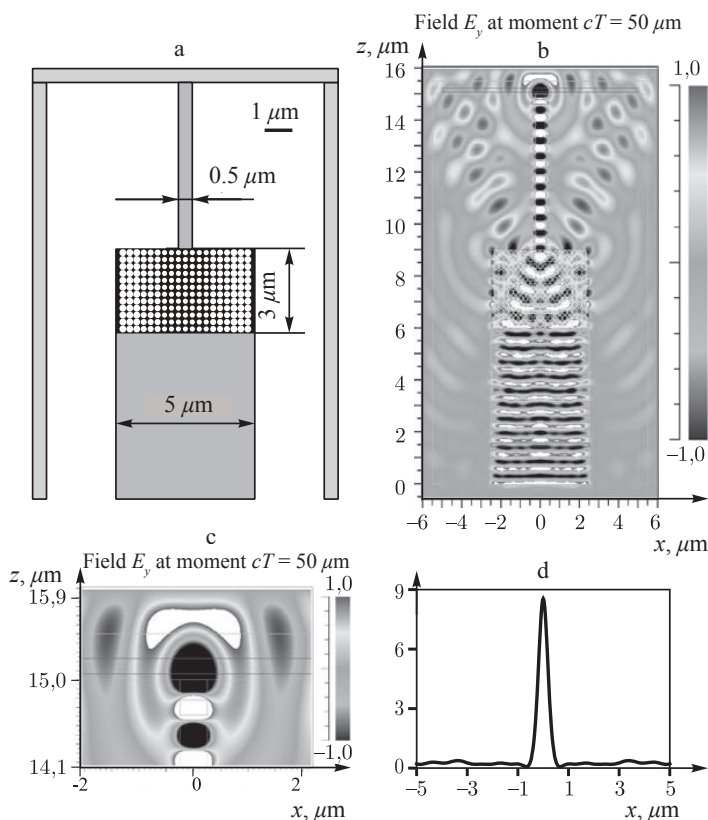


**Fig. 5.18.** Scheme of the coupling of two planar waveguides using PCGL (a), the instantaneous diffraction pattern of the TE-wave, calculated by FDTD using FullWAVE 6.0 program (b) and the enlarged fragment of the pattern at the output of the fibre  $0.5 \mu\text{m}$  wide (c), the intensity distribution at the exit of the fibre (d).

a narrow fibre is shown in Fig. 5.18d. Figure 5.18d shows that the diameter of the laser spot at the output ???at half intensity is??? is  $\text{FWHM} = 0.32\lambda$ . Note that the focus in the output waveguide  $1 \mu\text{m}$  wide (ceteris paribus) had a smaller diameter  $\text{FWHM} = 0.21\lambda$ , where  $\lambda$  is the wavelength in vacuum. This is lower than previously reported in [37] ( $\text{FWHM} = 0.24\lambda$ ).

**Simulation of the gap between the waveguides**

Figure 5.19 shows a 2D scheme of coupling of two coaxial waveguides with a gap between them. The width of the input waveguide with PCGL  $W_1 = 4.6 \mu\text{m}$ , the output  $W_2 = 1 \mu\text{m}$ , the gap between the waveguides  $\Delta z = 1 \mu\text{m}$ . Other parameters are:  $\lambda = 1.55 \mu\text{m}$ ,  $n = 1.46$ , PC-lens consists of a  $12 \times 17$  matrix of holes with a period of  $a = 0.25 \mu\text{m}$  and the hole diameter from 186 to 250 nm. Figure 5.19a shows in white the waveguide material ( $n = 1.46$ ), in black and gray the air ( $n = 1$ ). Figure 5.19b shows the instantaneous pattern of the amplitude  $E_y(x, z)$  for the TE-wave, calculated using FullWAVE 6.0 programme for the circuit in Fig. 5.19a. Figure 5.19c shows the

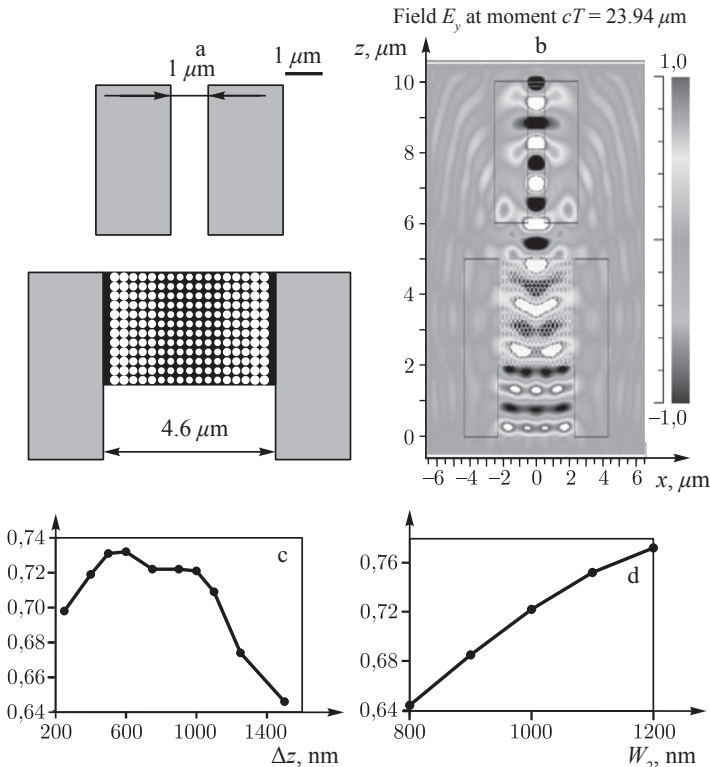


**Fig. 5.19.** 2D scheme of coupling between the two waveguides with PCGL at the gap  $\Delta z = 1 \mu\text{m}$  mm between the waveguides (white – material, black color – air) (a); instantaneous amplitude distribution  $E_y(x, z)$  of the TE-wave, calculated by FullWAVE (b); dependence of the effectiveness of coupling on the size the gap between the waveguides  $\Delta z$  (c) and the width of the output waveguide  $W_2$  (g).

dependence of the effectiveness of coupling (the ratio of the intensity of light at the exit of the narrow waveguide  $I$  to the intensity at the entrance to the wide waveguide  $I_0$ ) on the distance between the waveguides  $\Delta z$ . Figure 5.19c shows that the most effective coupling of 73% is achieved at the gap between the waveguides equal to  $0.6 \mu\text{m}$ . Note that in the gap between the waveguides there is the waveguide material ( $n = 1.46$ ) and not air.

Figure 5.19d shows the calculated dependence of the efficiency of coupling for the case shown in Fig. 5.19a on the width of the output waveguide  $W_2$  at the gap size of  $\Delta z = 1 \mu\text{m}$ . Figure 5.19d shows that with increasing width of the output waveguide  $W_2$  the efficiency of coupling almost linearly increases.

### Production of two 2D waveguides connected by PCGL

Planar waveguides by the scheme in Fig. 5.19a were recorded on a PMMA resist by direct writing technology with an electron beam at a voltage of 30 kV with a lithograph ZEP520A (University of St Andrews, Scotland). Processing of the resist in order to eliminate sections ‘illuminated’ by the electron beam was carried out using xylene. After that, the mixture of gases  $\text{CHF}_3$  and  $\text{SF}_6$  and the technology of reactive ion etching (RIE) were used for further plasma etching of the materials. That is, the pattern of 2D waveguides with PCGL (Fig. 5.19a) was transferred to a silicon film (SOI technology SOI: silicon-on-insulator): a silicon film 220 nm thick on a fused silica layer with thickness of  $2 \mu\text{m}$ . The etching depth was about 300 nm. The diameter of holes in the PCGL ranged from 160 nm to 200 nm. The length of the entire sample (length of the two waveguides) was 5 mm. Several similar structures were produced simultaneously on the same substrate differing in the gaps between the waveguides  $\Delta z = 0 \mu\text{m}$ ,  $1 \mu\text{m}$ ,  $3 \mu\text{m}$  and a few structures that differed in the offset between the axes of the two waveguides is  $\Delta x = 0 \mu\text{m}$ ,  $\pm 0.5 \mu\text{m}$ ,  $\pm 1 \mu\text{m}$ . Figure 5.20 shows a magnified (7000 times) photograph (top view) of two waveguides with an gap of  $\Delta z = 1 \mu\text{m}$  and with PCGL produced with a scanning electron microscope.

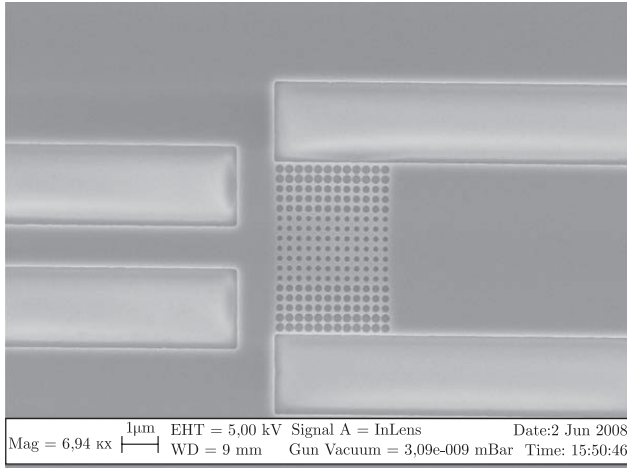
The parameters of the sample in Fig. 5.20 as the following. The design width of the waveguide  $W_1 = 4.5 \mu\text{m}$  and  $W_2 = 1 \mu\text{m}$ , PCGL consists of a  $12 \times 17$  matrix of holes with a period of 250 nm.

Figure 5.21 shows a part of the relief profile of the two waveguides fabricated in a silicon film on fused quartz (a) and a section of the matrix of  $6 \times 6$  holes of the PCGL (b) obtained with a scanning probe microscope.

Figure 5.22 shows the sections of the output (a) and input (b) waveguides. It is seen that the depth of etching of both waveguides is about the same and equal to 300 nm, and the width of the output waveguide at the tip is  $1 \mu\text{m}$ , and at the base  $2 \mu\text{m}$  (Fig. 5.22a). Similarly, the width of the input waveguide at the tip is  $4.5 \mu\text{m}$  and at the base of the trapezoid  $5 \mu\text{m}$  (Fig. 5.22b).

### Characterization of two waveguides with PCGL

Figure 5.23 shows the optical arrangement for the transmission spectrum of two planar waveguides connected by PCGL. The wideband light source (1450–1700 nm), operating on the basis of amplified spontaneous emission, is coupled with an optical fibre. The light at the output from the fibre is collimated and is incident on



**Fig. 5.20.** Photograph of planar waveguides made in a silicon film coupled with PCGL and obtained with a scanning electron microscope with a magnification of 7000.

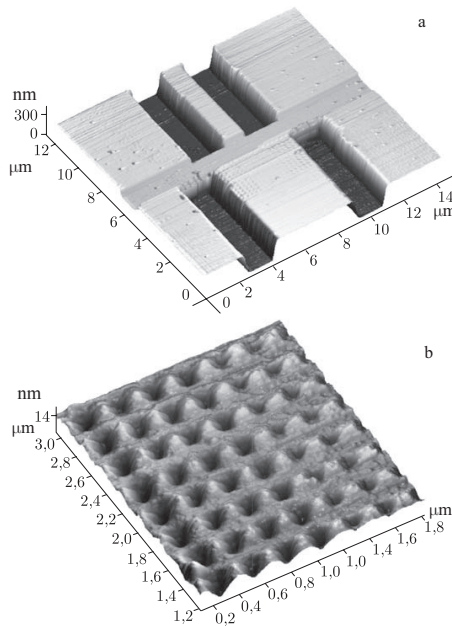


**Fig. 5.21.** Profile of the relief of fabricated 2D waveguides with PCGL obtained with a scanning probe microscope (atomic force microscope) SolverPro (Zelinograd): profile of waveguides (a), section 6×6 matrix of holes in PCGL (b). On the horizontal axes there are microns, on the vertical axis – nanometers.

a polarizer which separates TE-polarization. Further, using the microscope objective the radiation is focused on the surface of the input waveguide. A small fraction of light energy enters the waveguide and passes through the sample.

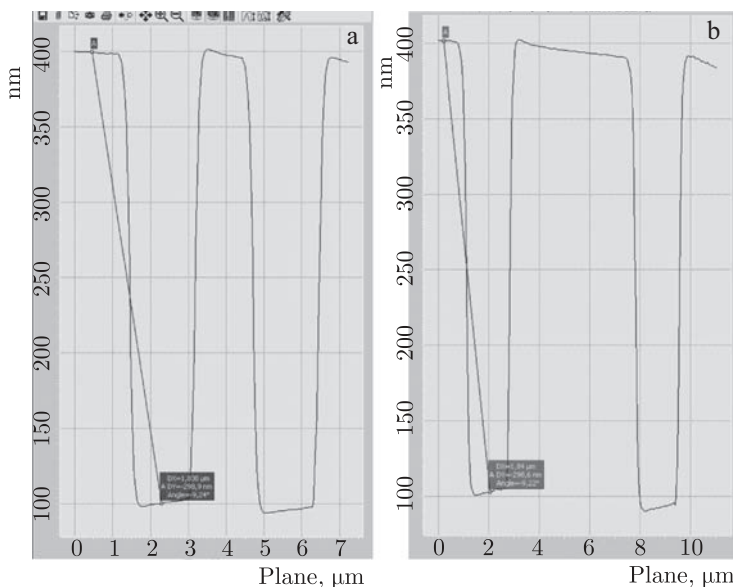


**Fig. 5.22.** Sections of the profile of the relief for narrow (a) and wide input (b) waveguides.

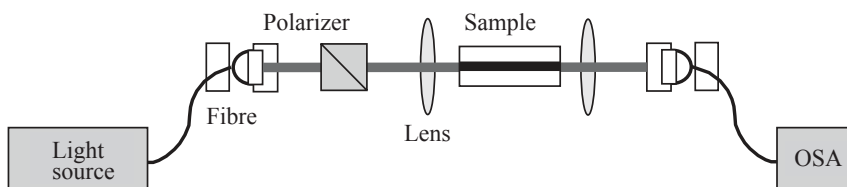


**Fig. 5.23.** Optical scheme for the investigation of nanophotonic devices, consisting of two waveguides and PCGL.

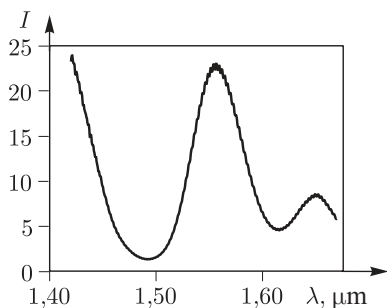


**Fig. 5.24.** The emission spectrum of the light source used in the optical system shown in Fig. 5.23.

At the exit of the narrow waveguide there is a second microlens, which gathers the light and focuses it on the input end of a multimode optical fibre connected to an optical spectrum analyzer (OSA). Figure 5.24 shows the spectrum of the radiation source, whose maximum is at the wavelength of  $1.55 \mu\text{m}$ . The intensity of radiation is given in arbitrary units.

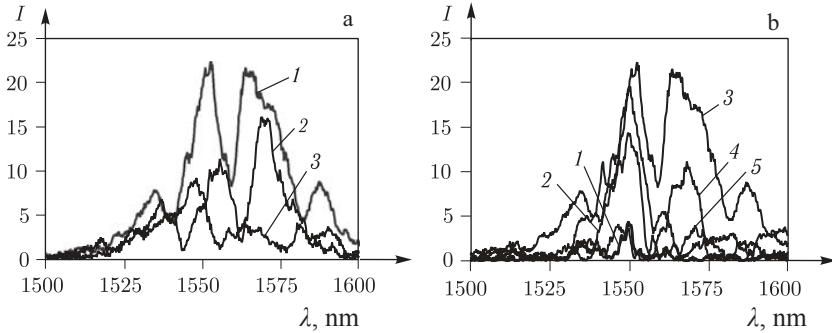


**Fig. 5.25.** The transmission spectra measured by the optical system shown in Fig. 5.23 for the samples shown in Fig. 5 and 6 at the following gaps between the waveguides (a):  $\Delta z = 0 \mu\text{m}$  (curve 1),  $\Delta z = 1 \mu\text{m}$  (curve 2) and  $\Delta z = 3 \mu\text{m}$  (curve 3), as well as at the following offsets from the optical axis of the output waveguide (b):  $\Delta x = 0 \mu\text{m}$  (curve 1),  $\Delta x = -0.5 \mu\text{m}$  (curve 2),  $\Delta x = +0.5 \mu\text{m}$  (curve 3),  $\Delta x = -1 \mu\text{m}$  (curve 4) and  $\Delta x = +1 \mu\text{m}$  (curve 5).

Figure 5.25 shows the transmission spectra of the samples in the range of 1.5–1.6  $\mu\text{m}$  at the following gaps  $\Delta z$  between the waveguides on the optical axis (a): 0  $\mu\text{m}$  (curve 1), 1  $\mu\text{m}$  (curve 2) and 3  $\mu\text{m}$  (curve 3), as well as the following displacement  $\Delta x$  from the optical axis of the output waveguide (B): 0  $\mu\text{m}$  (curve 1),  $-0.5 \mu\text{m}$  (curve 2),  $+0.5 \mu\text{m}$  (curve 3),  $-1 \mu\text{m}$  (curve 4) and  $+1 \mu\text{m}$  (curve 5). Figure 5.25a (curve 1) shows that the transmission spectrum has four local maxima at wavelengths around 1535 nm, 1550 nm, 1565 nm and 1590 nm. Two of these peaks (at wavelengths of 1550 nm and 1565 nm) have the intensity 3 times greater than the other two. This is most likely due to the fact that the intensity of radiation spectrum of the source (Fig. 5.24) is several times smaller at these wavelengths.

With increasing axial distance  $\Delta z = 1 \mu\text{m}$  between the waveguides (Fig. 5.25a, curve 2) the transmission spectrum on average retains its structure, but the local maxima decrease in magnitude and are shifted to the ‘red’ region of the spectrum. With further increase of the distance  $\Delta z = 3 \mu\text{m}$  between the waveguides (Fig. 5.25a, curve 3) the local maxima not only further decrease but also acquire a ‘blue’ shift. ‘Red’ shift is about 10 nm, and ‘blue’ shift is also  $-10 \text{ nm}$  (to a maximum near the central wavelength of 1.55  $\mu\text{m}$ ). Figure 5.25b shows that at the displacement of the output waveguide with the optical axis by 1  $\mu\text{m}$  (curves 4 and 5) the intensity of the output is reduced by 8 times (wavelength 1.55  $\mu\text{m}$ ). This means that the diameter of the focal spot, formed by PCGL in silicon, is less than 1  $\mu\text{m}$ .

To compare experiment with theory, we compared the transmission spectra. Figure 5.26 shows the smoothed experimental transmission spectrum (a) of the nanophotonic device (Fig. 5.20, but with no gap) and the calculated spectrum (b). Figure 5.26 shows that the two peaks of the spectrum in both cases occur at the same wavelengths (1535 nm and 1550 nm), the third maximum is shifted by 5 nm, and 4th maximum does not occur in the calculations. The standard deviation of the two spectra in Fig. 5.26 was 29%.

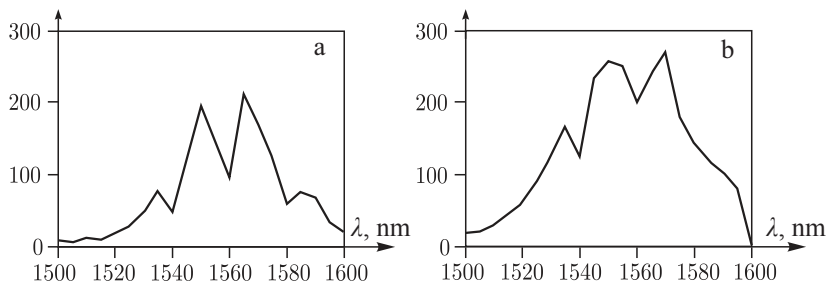


**Fig. 5.26.** The smoothed experimental (a) and calculated (b) transmission spectra for the two waveguides with PCGL without gaps (Fig. 5.20) in the wavelength range 1.5–1.6  $\mu\text{m}$ . The vertical axis – arbitrary units, horizontal axis – nanometers.

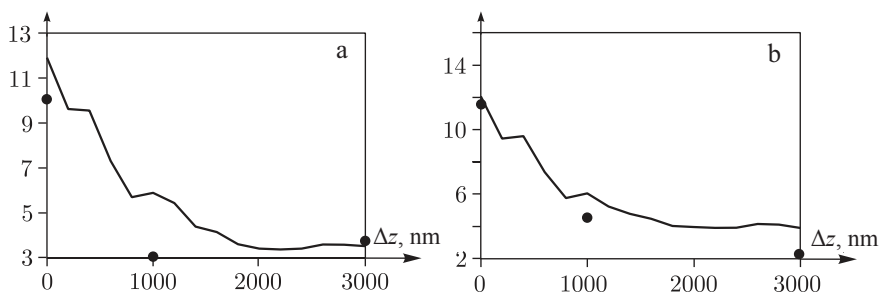


**Fig. 5.27.** Dependence of the transmission function of the two waveguides with PCGL on the gap between them  $\Delta z$  for the wavelengths 1550 nm (a) and 1565 nm (b): continuous curve – calculation, the individual dots – experiment. The vertical axis – arbitrary units along the abscissa – nanometers.

Another comparison between theory and experiment shown in Fig. 5.27. This figure shows the dependence of the transmission function of the device (Fig. 5.20) in arbitrary units on the distance  $\Delta z$  between two coaxial waveguides for the wavelengths of 1550 nm (a) and 1565 nm (b): the continuous curve shows the calculations and the experiments are indicated by individual dots.

Figure 5.27 shows that on average the calculations and experiments consistently reflect a decrease in the intensity at the output of the waveguide as the distance between the waveguides increases. Note that the experimental points (all except one) lie below the theoretical curve, which is caused by absorption of light in real waveguides with a length of 5 mm. Figure 5.27 also shows that the calculated curve of the output intensity is reduced by half when the gap between the waveguides is  $\Delta z = 600$  nm, which agrees with the longitudinal size of the focal spot of the PCGL (Fig. 5.16c).

### 5.3 Sharp focusing of radially-polarized light

A large number of optical devices use sharp focusing of laser light: optical memory drives, photolithography, confocal microscopy, optical micromanipulation. Studies of the formation of the minimum focal spot with superresolution extends are

continuing. The scalar paraxial theory of diffraction shows that the diameter of the focal spot of the Airy disk, the amplitude of which is described by the function  $2J_1(x)/x$  at half intensity??? is equal to  $\text{FWHM} = 0.51\lambda/\text{NA}$ , where  $\lambda$  is the wavelength of light, NA is the numerical aperture of the focusing lens. The area of the Airy disk at half intensity??? is  $\text{HMA} = 0.204^2$  (HMA = half maximum area) with  $\text{NA} = 1$ . This is the area of a two-dimensional region bounded by a closed curve drawn in the focal plane of the diffraction pattern at the points where the light intensity is equal to half the maximum value. If we use a narrow annular aperture and a spherical lens to form a diffraction pattern, which describes the Bessel function  $J_0(x)$ , then the diameter of the focal spot is smaller  $\text{FWHM} = 0.36\lambda/\text{NA}$ . The diameter of the focal spot at sharp focused light depends on the type of polarization of the beam and the type of optical element, performing focusing. It has been experimentally shown [57] that with the help of a Leico microlens plan apo 100x with  $\text{NA} = 0.9$  in the air the laser beam with radial polarization can be focused to a spot with the area  $\text{HMA} = 0.16\lambda^2$  and the diameter  $\text{FWHM} = 0.451\lambda$ . This is carried out using the fundamental mode of a helium–neon laser with a wavelength of 632.8 nm and a ring-shaped amplitude mask, covering the centre part 3 mm in diameter of the incident beam with a diameter 3.6 mm. In [57] it is also indicated that, in theory, for a laser beam with linear polarization of the field in the same conditions we can expect that the focal spot will have a large area of  $\text{HMA} = 0.26\lambda^2$  and larger diameter  $\text{FWHM} = 0.575\lambda$ . If the beam is circularly polarized,  $\text{HMA} = 0.22\lambda^2$ . Note that if the focal spot is circular, the  $\text{HMA} = \pi D^2/4$ , where  $\text{FWHM} = D$ .

Most works on modelling of sharp focusing of the laser beam use the Debye vector theory or the analogous Richards–Wolf theory. In these theories, the electromagnetic field in the image of a point source, situated at infinity, by the aplanatic optical system is expressed in integral form as an expansion in plane waves. Some studies use the Rayleigh–Sommerfeld diffraction theory. Thus, in [28] on the basis of the Debye formulas that are true if the focal length is much larger than the wavelength, it is shown that with the aid of a parabolic mirror or a flat diffractive lens with numerical aperture  $\text{NA} = 0.98$  the radially polarized hollow Gaussian beam with the amplitude  $r \exp(-r^2/w^2)$ , where  $r$  is the radial coordinate,  $w$  is the waist radius of the Gaussian beam, can be focused by an aplanatic lens in the focal spot with the area of  $\text{HMA} = 0.210\lambda^2$  and  $\text{HMA} = 0.157\lambda^2$  respectively. It was also calculated [58] that for a parabolic mirror with a numerical aperture  $\text{NA} = 1$  the area of the focal spot is less than  $\text{HMA} = 0.154\lambda^2$ . And if the Gaussian beam is restricted by a narrow annular aperture, the area of the focal spot will be even less  $\text{HMA} = 0.101\lambda^2$ .

In [59] attention is given to the non-paraxial propagation of spirally polarized Laguerre–Gauss beams (LG). It is shown that such beams are also candidates for sharp focusing. To obtain radially-polarized laser beams, we can use a conventional interferometer with two phase steps in its ???, giving a delay at wave half length and rotated relative to each other by  $90^\circ$  around the optical axis [60]. In [61], the Richards–Wolf (RW) formula is used to simulate focusing of a linearly polarized beam with a planar aplanatic lens with a high numerical aperture with an annular (2 or 3 rings) stepped phase mask. The parameters of the mask at which superresolution by 20% along the optical axis is achieved. Using the RW formulas, in [62] it is

shown that by focusing radially-polarized  $\text{TEM}_{11}$  laser mode, which has two light rings in its cross-section, with the help of an aplanatic lens with  $\text{NA} = 1.2$  in water ( $n = 1.33$ ) a dark area appears in the focal region surrounded on all sides by light (optical bottle). The longitudinal dimension of this field is  $2\lambda$ , and transverse is  $\lambda$ . In [63], using the RW-formulas the authors considered optimal distribution of the optical vortex with circular polarization. It is shown that at the topological charge  $n = 1$  and the choice of such a sign that the spiral spin of the phase of an optical vortex compensates the rotation of the polarization in the opposite direction, in the focal plane ( $\text{NA} = 0.9$ ) there is a circular focal spot with the diameter smaller than the wavelength.

With the help of the Rayleigh–Sommerfeld (RS) integral the authors of [64] studied the non-paraxial propagation of the LG modes with radial polarization but no spiral phase component. It is shown that when the non-paraxiality parameter  $f = (kw)^{-1}$ , where  $k$  is the wavenumber of light,  $w$  is the constriction of the Gaussian beam, is selected equal to 0.5, the light spot diameter at the Fresnel distance from the waist is about  $0.4\lambda$  for  $p = 3$ , where  $p$  is the order of the Laguerre polynomial. In [65] the Maxwell's equations in the cylindrical coordinates are solved using a series expansion of the non-paraxiality parameter  $f = \theta/2$ , where  $\theta$  is the angle of diffraction, with the accuracy up to  $\theta^5$ . As an example we consider the diffraction of the beam of the axicon–Gauss type. It is shown that at the diffraction angle  $\theta = 0.75^\circ$  the waist radius is  $0.424\lambda$ . On the basis of the RS-integral analytical expressions were obtained in [66] describing the non-paraxial propagation of the elegant LG modes in the cross section of which there is always an annular intensity distribution. In [67] the authors reported on a new form of resist for lithography PMMA-DR1, which has polarization-filtering properties and responds only to the longitudinal component of the electric vector of the electromagnetic wave. It was shown experimentally that a radially-polarized beam of an argon laser  $\lambda = 514$  nm, passing an axicon with  $\text{NA} = 0.67$ , forms a focal spot with a diameter  $\text{FWHM} = 0.89\lambda$ , but after writing on the resist a spot with the size of  $0.62\lambda$  forms.

Using the RW formulas it is shown in [68] that radially polarized higher laser modes  $\text{R-TEM}_{p1}$  can reduce the diameter of the focal spot. Thus, when  $\text{NA} = 1$ , and by focusing with aplanatic lenses for numbers of the modes  $p = 0, 1, 2, 3$ , we obtain focal spots with a diameter of  $\text{FWHM} = 0.582\lambda, 0.432\lambda, 0.403\lambda, 0.378\lambda$ . In [69] using the RW formulas attention is given to vector diffraction and focusing by an aplanatic lens of a linearly-polarized beam with elliptical radial symmetry with an eccentricity of 0.87. The numerical aperture was  $\text{NA} = 0.9$ . In this case an elliptical focal spot area of  $\text{HMA} = 0.56\lambda^2$  formed. In [70] the non-paraxial propagation (5<sup>th</sup> order corrections) of radially-polarized LG beams  $\text{R-TEM}_{p1}$  was studied. It is shown that when the angle of diffraction  $\theta = 2(kw)^{-1}$  is more than 0.5 the non-paraxial corrections of 5<sup>th</sup> order are no longer sufficient to describe the mode  $\text{R-TEM}_{21}$ . In [71] using the RW formula it is shown that when illuminating the exit pupil of a spherical lens with plane, Gaussian or Bessel–Gaussian beams of radially-polarized light the localized focal spot diameter is equal to  $\text{FWHM} = 0.6\lambda, 1.2\lambda, 1.4\lambda$  respectively, at  $\text{NA} = 1.4, \lambda = 632.8$  nm,  $n = 1.5$ . In [72] also using the RW formulas it is shown that for the incident radially polarized Bessel–Gaussian beam  $J_1(2r)\exp(-r^2)$

and a binary phase Fresnel plate the focal spot has a diameter of  $\text{FWHM} = 0.425\lambda/\text{NA}$ . When a three-zone optimized plate was added to the Fresnel zone plate, the resultant diameter of the focal spot was even smaller,  $\text{FWHM} = 0.378\lambda/\text{NA}$ .

With the help of a parabolic mirror with a diameter of 19 mm and  $\text{NA} = 0.999$ , and with a radially polarized laser beam with a wavelength of 632.8 nm the authors of [73] experimentally obtained a focal spot with the least to date area of  $\text{HMA} = 0.134\lambda^2$ . Radial polarization was obtained from the linear polarization of the laser beam with four half-wave plates, arranged in four quadrants of the aperture of the beam and rotated by  $45^\circ$  (along the bisector in each quadrant). The incident beam had an Bessel–Gauss amplitude. Modelling was carried out with the aid of the Debye formulas. The distribution of the intensity in the focal plane was measured with a fluorescent bulb with a diameter of 40 nm. For comparison, recall that the radius of the Airy disk in the scalar approximation is equal to  $0.61\lambda$  at  $\text{NA} = 1$ , and in [73] a focal spot with a radius from maximum to first minimum was equal to  $0.45\lambda$ . Recall that the best experimental results for aplanatic lenses is  $\text{HMA} = 0.16\lambda^2$  [57].

In [74] the authors proposed and experimentally tested a method way to convert linear polarization to radial or azimuthal using photonic crystal fibre of length 24 mm. In [75] calculations were carried out to determine the forces acting from the the focused laser beams ( $\text{NA} = 1.25$  in water, angle of convergence  $140^\circ$ ) on a spherical particle with the refractive index  $n = 1.59$  and a radius equal to  $4\lambda/n$ . Several types of incident beams were considered: Gaussian, LG mode with radial, azimuthal and circular polarization. It was found that the efficiency of optical trapping is higher for radial polarization of light beams. In [76] the authors investigated numerically and experimentally a radially polarized laser beam, which is focused through a uniaxial crystal at the output of a Nd laser with a hemispherical cavity.

An interesting result was obtained in [77], where with the aid of the Debye formula it was shown that radially-polarized LG modes of even orders  $\text{LG}_p^0$  with numerical aperture  $\text{NA} = 0.85$  after passage through a special ring amplitude mask are focused in a small focal spot with almost no side lobes, with the area at  $\text{HMA} = 0.276\lambda^2$ . Using the amplitude mask does not reduce the size of the focal spot, but reduces the level of side lobes in the focal diffraction pattern and also five times the depth of field.

In [78] the scalar version of the RW formulas was used for analytical investigation of the function of the output pupil optimum for obtaining high resolution. In the two-dimensional case, a photonic crystal lens can be used for the radiation propagating in a planar waveguide and to focus this radiation at the output of the waveguide. In [56] it is shown that the 2D photonic crystal lens, which implements a gradient Michaelian microlens (refractive index decreases according to the function  $\text{sekons}$ ), allows to focus the laser light in a focal spot smaller than that predicted by the scalar theory. In the paraxial case, the two-dimensional diffraction pattern in focus is described by the sinc-function for which  $\text{FWHM} = 0.44\lambda/\text{NA}$ .

The photonic crystal lens can also be used to produce a spot with a diameter of  $\text{FWHM} = 0.42\lambda$  with numerical aperture  $\text{NA} = 0.67$ . In [79], the FDTD method is applied to simulate the focusing of linearly polarized microwave radiation with a frequency of 30 GHz (wavelength  $\lambda = 10$  mm) with binary phase Fresnel lenses

made of a material with a dielectric constant  $\varepsilon = 4$ . Focal spots for different lenses were formed at distances of  $2\lambda$ ,  $\lambda$  and  $0.5\lambda$  from the flat surface of the Fresnel lens and had the respective diameters:  $1.04\lambda$ ,  $0.90\lambda$  and  $0.80\lambda$  (here the diameter is twice the radius of the maximum intensity to the first minimum). The shape of the focal spot was close to a square.

In this section, using the R-FDTD-method, which applies to the radially symmetric case, we review the results of simulation of sharp focusing of a plane electromagnetic wave with linear, azimuthal and radial polarization using the micro-optics element: a biconvex spherical lenses, gradient lenses and conical axicon. It is shown that the smallest focal spot can be achieved by focusing a radially-polarized ring-shaped Gaussian beam on a micro-axicon with a numerical aperture  $NA = 0.65$ . The area of the focal spot at half intensity is  $HMA = 0.096\lambda^2$ , and the diameter of  $FWHM = 0.35\lambda$ .

### 5.3.1. Richards–Wolf vector formulas

According to the vector Debye theory, the vector of the strength of the electric field of the electromagnetic wave in the focal region in cylindrical coordinates ( $r$ ;  $\psi$ ,  $z$ ) is expressed through the amplitude  $l(\theta)$  of a converging spherical wave in the coordinates of the exit pupil of the aplanatic optical system in the form of (linear polarization vector is directed along the axis  $y$ ):

$$E_x(r, \psi, z) = \frac{-iA}{2\pi} \int_0^\alpha d\theta \int_0^{2\pi} d\phi \sin\theta \sqrt{\cos\theta} \sin 2\phi \times \quad (5.30)$$

$$\times (1 - \cos\theta) l(\theta) \exp[ikz \cos\theta - ikr \sin\theta \cos(\psi - \phi)],$$

$$E_y(r, \psi, z) = \frac{iA}{2\pi} \int_0^\alpha d\theta \int_0^{2\pi} d\phi \sin\theta \sqrt{\cos\theta} \times \quad (5.31)$$

$$\times [(1 + \cos\theta) + (1 - \cos\theta) \cos 2\phi] \times$$

$$\times l(\theta) \exp[ikz \cos\theta - ikr \sin\theta \cos(\psi - \phi)],$$

$$E_z(r, \psi, z) = \frac{iA}{\pi} \int_0^\alpha d\theta \int_0^{2\pi} d\phi \sin^2\theta \sqrt{\cos\theta} \cos\phi \times \quad (5.32)$$

$$\times l(\theta) \exp[ikz \cos\theta - ikr \sin\theta \cos(\psi - \phi)],$$

where  $A$  is a constant,  $\alpha = \arcsin(NA)$ ,  $k$  is the wavenumber of the light. For example, a Gaussian function in the pupil plane will have the form:

$$l(\theta) = \exp\left(\frac{-\rho^2}{w^2}\right) = \exp\left[-\left(\frac{\beta \sin\theta}{\sin\alpha}\right)^2\right], \quad (5.33)$$

where  $\beta$  is a constant.

Richards and Wolf, on the basis of the Debye formulas (5.30)–(5.32) obtained simpler formulas, integrating with respect to the azimuthal angle  $\phi$  for radially-polarized light [80]:

$$E_r(r, z) = A \int_0^\alpha \sin 2\theta \sqrt{\cos \theta} l(\theta) \exp[ikz \cos \theta] J_1(kr \sin \theta) d\theta, \quad (5.34)$$

$$E_z(r, z) = 2iA \int_0^\alpha \sin^2 \theta \sqrt{\cos \theta} l(\theta) \exp[ikz \cos \theta] J_0(kr \sin \theta) d\theta, \quad (5.35)$$

where  $J_0(x)$  and  $J_1(x)$  are Bessel functions. Equations (5.34) and (5.35) show that the radially-polarized wave does not depend on the angle  $\psi$ , has only two electrical components  $E_r$  and  $E_z$ , and it can also be seen that  $E_r(r=0) = 0$  for any  $z$  and any function  $l(\theta)$ . The focus is at the origin of the coordinates  $(r, \psi, z) = (0, \psi, 0)$ . When replacing an aplanatic lens by a Fresnel zone plate, instead of the factor  $(\cos \theta)^{1/2}$  in (5.34) and (5.35) we should use another factor  $(\cos \theta)^{-3/2}$  [58].

In the Cartesian coordinates for linearly polarized light (polarization vector is directed along the axis  $y$ ) the RW formulas take the form:

$$E_x(r, \psi, z) = -iA \sin 2\psi \int_0^\alpha \sin \theta \sqrt{\cos \theta} \times \\ \times l(\theta)(1 - \cos \theta) \exp[ikz \cos \theta] J_2(kr \sin \theta) d\theta, \quad (5.36)$$

$$E_y(r, \psi, z) = -iA \cos 2\psi \int_0^\alpha \sin \theta \sqrt{\cos \theta} l(\theta)(1 - \cos \theta) \exp[ikz \cos \theta] J_2(kr \sin \theta) d\theta - \\ -iA \int_0^\alpha \sin \theta \sqrt{\cos \theta} l(\theta)(1 + \cos \theta) \exp[ikz \cos \theta] J_0(kr \sin \theta) d\theta, \quad (5.37)$$

$$E_z(r, \psi, z) = -2A \cos \psi \int_0^\alpha \sin^2 \theta \sqrt{\cos \theta} \times \\ \times l(\theta) \exp[ikz \cos \theta] J_1(kr \sin \theta) d\theta. \quad (5.38)$$

In the case of azimuthal polarization of light instead of the radial component  $E_r$  in (5.34) the azimuthal component of the electric field differs from zero:

$$E_\psi(r, z) = 2A \int_0^\alpha \sin \theta \sqrt{\cos \theta} l(\theta) \exp[ikz \cos \theta] J_1(kr \sin \theta) d\theta. \quad (5.39)$$

From (5.35) and (5.39) it can be seen that the azimuthally polarized wave does not depend on angle  $\psi$ . These formulas (5.30)–(5.39) were used for simulation in [57, 58, 61–63, 66, 68, 69, 71–73, 75, 77], studying the sharp focusing of laser light.

### 5.3.2. The minimum focal spot: an analytical assessment

In [78] the intensity distribution of light at the focus of a radially-symmetrical optical system with high numerical aperture is analyzed using the scalar form of the RW formula:

$$U(r, z) = -ikf \int_0^\alpha P(\theta) \exp[ikz \cos \theta] J_0(kr \sin \theta) d\theta, \quad (5.40)$$

where  $U(r, z)$  is the complex amplitude of the light near the focus,  $P(\theta)$  is the function of the pupil of the optical system,  $f$  is the focal length. If we compare (5.40) with (5.35) for the longitudinal component of the radially-polarized light, we can conclude that the scalar amplitude, describing the non-paraxial focusing of light (5.40), is proportional to the longitudinal component of a converging spherical wave with radial polarization (5.35). Using the reference integrals in [81], we can estimate the minimum possible diameter at the focal spot of the non-paraxial optical system. Using the reference integral

$$\int_0^\pi \left\{ \begin{array}{l} \sin(bx) \\ \cos(bx) \end{array} \right\} J_\nu(c \sin x) dx = \pi \left\{ \begin{array}{l} \sin(b\pi/2) \\ \cos(b\pi/2) \end{array} \right\} J_{(\nu-b)/2}(c/2) J_{(\nu+b)/2}(c/2), \quad (5.41)$$

and setting in (5.40)  $P(\theta) = \sin \theta$ ,  $\alpha = \pi$ , and in (5.41)  $\nu = 0$ ,  $b = 1$ ,  $c = kr$ , we obtain from equation (5.40) for the uniform pupil in the focal plane  $z = 0$  the following complex amplitude:

$$U_1(r, z = 0) = -2ikf \sin(kr) / (kr). \quad (5.42)$$

It follows from equation (5.42) that the minimum focal spot diameter (twice the distance from the maximum to first minimum) is

$$D_1 = \lambda, \quad (5.43)$$

and the diameter of the focal spot ??? is  $\text{FWHM} = 0.44\lambda$ , and the spot area ??? is  $\text{HMA} = 0.152\lambda^2$ . The latter figure is consistent with the calculations in [58].

The result with the same order of magnitude can be obtained by choosing a uniform pupil function in the form of  $P(\theta) = 1$ . Then instead of (5.40) with (5.41) we obtain ( $\nu = 0$ ,  $b = 0$ ):

$$U_2(r, z = 0) = -ikf \pi J_0^2(kr/2). \quad (5.44)$$

From (5.44) it follows that in this particular case, the focal spot diameter (twice the distance from the maximum to first minimum of intensity) is equal to

$$D_2 = 1.53\lambda. \quad (5.45)$$

If the focusing lens is illuminated with a narrow annular field with the pupil function  $P(\theta) = \delta(\theta - \alpha)$ , then from (5.40) we obtain for the amplitude in the focus:

$$U_3(r, z = 0) = -2ikfJ_0(krNA). \quad (5.46)$$

From (5.46) it follows that the diameter of the focal spot, similar to (5.43) and (5.45) is equal to ( $NA = 1$ )

$$D_3 = 0.76\lambda, \quad (5.47)$$

and the diameter of such a focal spot ??? is  $\text{FWHM} = 0.36\lambda$ , and the spot area ??? is  $\text{HMA} = 0.101\lambda^2$ . The latter figure is consistent with the calculations in [58].

The formulas (5.43) (5.45) and (5.47) give only an estimate of the minimum diameter of the focal spot with a scalar formula (5.40), but in sharp focusing it is required to take into account the vector nature of the field, when all three components of the electric field give a comparable contribution to the formation of focal pattern. The value of (5.47) can be considered as the accurate minimum diameter of the focal spot, which can be formed by the focusing optical system illuminated by radially-polarized light. This follows from the fact that the scalar equation (5.40) coincides with the expression for the longitudinal component of the field (5.35), while the radial component (5.34) of radially-polarized light at the optical axis is zero. But the Debye and Richards–Wolf formulas are approximate (they were obtained under the condition that the focal length of the optical system is much larger than the wavelength), therefore we will consider the rigorous solution of the diffraction problem on the basis of the numerical solution of Maxwell's equations. Only at the exact solution of the diffraction problem, and if the focal length is comparable to the wavelength, can we hope to obtain the area of the focal spot smaller than  $\text{HMA} = 0.101\lambda^2$ .

### 5.3.3. Maxwell's equations in cylindrical coordinates

In [82] a method was proposed for calculating diffraction of the electromagnetic wave on a radially symmetric optical element on the basis of the difference solution of Maxwell's equations in cylindrical coordinates. The Maxwell's equations in the cylindrical coordinates ( $r, \phi, z$ ) in SI units are as follows:

$$\frac{1}{r} \frac{\partial H_z}{\partial \phi} - \frac{\partial H_\phi}{\partial z} = \varepsilon \varepsilon_0 \frac{\partial E_r}{\partial t} + \sigma E_r, \quad (5.48)$$

$$\frac{\partial H_r}{\partial z} - \frac{\partial H_z}{\partial r} = \varepsilon \varepsilon_0 \frac{\partial E_\phi}{\partial t} + \sigma E_\phi, \quad (5.49)$$

$$\frac{1}{r} \frac{\partial(rH_\phi)}{\partial r} - \frac{1}{r} \frac{\partial H_r}{\partial \phi} = \varepsilon \varepsilon_0 \frac{\partial E_z}{\partial t} + \sigma E_z, \quad (5.50)$$

$$\frac{1}{r} \frac{\partial E_z}{\partial \phi} - \frac{\partial E_\phi}{\partial z} = -\mu \mu_0 \frac{\partial H_r}{\partial t}, \quad (5.51)$$

$$\frac{\partial E_r}{\partial z} - \frac{\partial E_z}{\partial r} = -\mu \mu_0 \frac{\partial H_\phi}{\partial t}, \quad (5.52)$$

$$\frac{1}{r} \frac{\partial(rE_\phi)}{\partial r} - \frac{1}{r} \frac{\partial E_r}{\partial \phi} = -\mu \mu_0 \frac{\partial H_z}{\partial t}, \quad (5.53)$$

where  $\mu$  and  $\varepsilon$  are relative magnetic and electric permeability,  $\mu_0$  and  $\varepsilon_0$  are magnetic and electric permittivity of vacuum,  $\sigma$  is conductivity,  $E_v$  and  $H_v$  are the intensity of the electric and magnetic fields, the index  $v$  takes the values  $r, \phi, z$ . We expand the components of the electromagnetic field in a Fourier series in the azimuthal angle  $\phi$ :

$$E_\gamma(r, z, \phi, t) = \frac{E_{\gamma 0}(r, z, t)}{2} + \sum_{k=1}^{\infty} \left[ E_{\gamma, k}^{(1)}(r, z, t) \cos(k\phi) + E_{\gamma, k}^{(2)}(r, z, t) \sin(k\phi) \right], \quad (5.54)$$

$$H_\gamma(r, z, \phi, t) = \frac{H_{\gamma 0}(r, z, t)}{2} + \sum_{k=1}^{\infty} \left[ H_{\gamma, k}^{(1)}(r, z, t) \cos(k\phi) + H_{\gamma, k}^{(2)}(r, z, t) \sin(k\phi) \right]. \quad (5.55)$$

Substituting (5.54) and (5.55) into (5.48)–(5.53), we can calculate the derivatives of  $\phi$ . Then instead of (5.48)–(5.53) for  $k = 0$ , we have six of the Maxwell equations in the functions that do not depend on the angle  $\phi$ :

$$-\frac{\partial H_{\phi, 0}}{\partial z} = \varepsilon \varepsilon_0 \frac{\partial E_{r, 0}}{\partial t} + \sigma E_{r, 0}, \quad (5.56)$$

$$\frac{\partial H_{r, 0}}{\partial z} - \frac{\partial H_{z, 0}}{\partial r} = \varepsilon \varepsilon_0 \frac{\partial E_{\phi, 0}}{\partial t} + \sigma E_{\phi, 0}, \quad (5.57)$$

$$\frac{1}{r} \frac{\partial(rH_{\phi, 0})}{\partial r} = \varepsilon \varepsilon_0 \frac{\partial E_{z, 0}}{\partial t} + \sigma E_{z, 0}, \quad (5.58)$$

$$-\frac{\partial E_{\phi,0}}{\partial z} = -\mu\mu_0 \frac{\partial H_{r,0}}{\partial t}, \quad (5.59)$$

$$\frac{\partial E_{r,0}}{\partial z} - \frac{\partial E_{z,0}}{\partial r} = -\mu\mu_0 \frac{\partial H_{\phi,0}}{\partial t}, \quad (5.60)$$

$$\frac{1}{r} \frac{\partial (rE_{\phi,0})}{\partial r} = -\mu\mu_0 \frac{\partial H_{z,0}}{\partial t}. \quad (5.61)$$

At an arbitrary integer  $k \neq 0$ , the amplitudes of the angular harmonics  $E^{(1)}$ ,  $E^{(2)}$ ,  $H^{(1)}$  and  $H^{(2)}$  from (5.54) and (5.55) are related by the following 12 equations:

$$-\frac{1}{r} kH_{z,k}^{(1)} - \frac{\partial H_{\phi,k}^{(2)}}{\partial z} = \varepsilon\varepsilon_0 \frac{\partial E_{r,k}^{(2)}}{\partial t} + \sigma E_{r,k}^{(2)}, \quad (5.62)$$

$$\frac{\partial H_{r,k}^{(2)}}{\partial z} - \frac{\partial H_{z,k}^{(2)}}{\partial r} = \varepsilon\varepsilon_0 \frac{\partial E_{\phi,k}^{(2)}}{\partial t} + \sigma E_{\phi,k}^{(2)}, \quad (5.63)$$

$$\frac{1}{r} \frac{\partial (rH_{\phi,k}^{(2)})}{\partial r} - \frac{1}{r} kH_{r,k}^{(1)} = \varepsilon\varepsilon_0 \frac{\partial E_{z,k}^{(2)}}{\partial t} + \sigma E_{z,k}^{(2)}, \quad (5.64)$$

$$-\frac{1}{r} kE_{z,k}^{(1)} - \frac{\partial E_{\phi,k}^{(2)}}{\partial z} = -\mu\mu_0 \frac{\partial H_{r,k}^{(2)}}{\partial t}, \quad (5.65)$$

$$\frac{\partial E_{r,k}^{(2)}}{\partial z} - \frac{\partial E_{z,k}^{(2)}}{\partial r} = -\mu\mu_0 \frac{\partial H_{\phi,k}^{(2)}}{\partial t}, \quad (5.66)$$

$$\frac{1}{r} \frac{\partial (rE_{\phi,k}^{(2)})}{\partial r} - \frac{1}{r} kE_{r,k}^{(1)} = -\mu\mu_0 \frac{\partial H_{z,k}^{(2)}}{\partial t}, \quad (5.67)$$

$$-\frac{1}{r} kH_{z,k}^{(2)} - \frac{\partial H_{\phi,k}^{(1)}}{\partial z} = \varepsilon\varepsilon_0 \frac{\partial E_{r,k}^{(1)}}{\partial t} + \sigma E_{r,k}^{(1)}, \quad (5.68)$$

$$\frac{\partial H_{r,k}^{(1)}}{\partial z} - \frac{\partial H_{z,k}^{(1)}}{\partial r} = \varepsilon\varepsilon_0 \frac{\partial E_{\phi,k}^{(1)}}{\partial t} + \sigma E_{\phi,k}^{(1)}, \quad (5.69)$$

$$\frac{1}{r} \frac{\partial (rH_{\phi,k}^{(1)})}{\partial r} - \frac{1}{r} kH_{r,k}^{(2)} = \varepsilon\varepsilon_0 \frac{\partial E_{z,k}^{(1)}}{\partial t} + \sigma E_{z,k}^{(1)}, \quad (5.70)$$

$$-\frac{1}{r} kE_{z,k}^{(2)} - \frac{\partial E_{\phi,k}^{(1)}}{\partial z} = -\mu\mu_0 \frac{\partial H_{r,k}^{(1)}}{\partial t}, \quad (5.71)$$

$$\frac{\partial E_{r,k}^{(1)}}{\partial z} - \frac{\partial E_{z,k}^{(1)}}{\partial r} = -\mu\mu_0 \frac{\partial H_{\phi,k}^{(1)}}{\partial t}, \quad (5.72)$$

$$\frac{1}{r} \frac{\partial (rE_{\phi,k}^{(1)})}{\partial r} - \frac{1}{r} kE_{r,k}^{(2)} = -\mu\mu_0 \frac{\partial H_{z,k}^{(1)}}{\partial t}. \quad (5.73)$$

Note that in [82] of the 12 equations (5.62)–(5.73) only six equations are considered. The number of equations (5.62)–(5.73) could be reduced if the optical element on which diffraction is considered has a cylindrical symmetry and if the an electromagnetic wave with linear, radial or azimuthal polarization falls in the normal direction on this optical element (Fig. 5.28).

Linear polarization of the incident wave (let  $E^{\text{inc}} = E_y$ ) means that at each point in the cross section the electric vector is directed along the axis  $y$  (Fig. 5.28a). In the case of azimuthal polarization the electric vector at any point in the incident wave is directed along the tangent to the circles whose centres lie on the optical axis (Fig. 5.28b). In the case of radial polarization the electric vector at any point of the section of the incident wave is directed along the radii of the circles whose centres lie on the optical axis which coincides with the symmetry axis of the optical element (Fig. 5.28c).

### 5.3.4. Maxwell's equations for the incident wave with linear polarization

Consider the normal incidence of an electromagnetic wave with linear polarization in the initial plane  $z = 0$ . Then the electric vector of this wave will have only

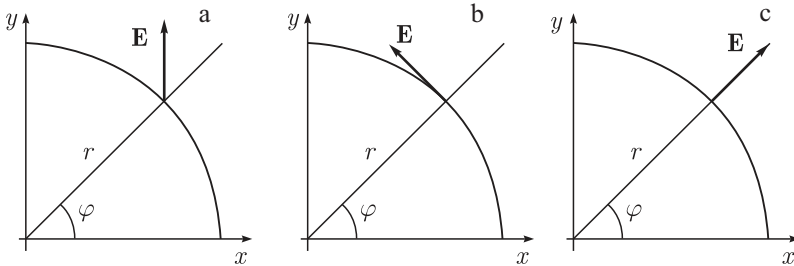


**Fig. 5.28.** Incident radiation on the optical element has linear (a), azimuthal (b) or radial (c) polarization.

one projection  $E_y^{\text{inc}} = E_0(r) \cos(\omega t)$ , where  $\omega$  is the angular frequency of a monochromatic wave,  $E_0(r)$  is the amplitude of the wave in the plane  $z = 0$ . We express the incident field  $E_y$  through the cylindrical components:

$$E_r = E_y \sin \phi, \quad E_\phi = E_y \cos \phi \quad (5.74)$$

or in the notation (5.54) (5.55):

$$E_r = E_{r,1}^{(2)} \sin \phi, \quad E_\phi = E_{\phi,1}^{(1)} \cos \phi. \quad (5.75)$$

Thus, from equations (5.62) - (5.73) there are only six equations:

$$-\frac{1}{r} H_{z,1}^{(1)} - \frac{\partial H_{\phi,1}^{(2)}}{\partial z} = \varepsilon \varepsilon_0 \frac{\partial E_{r,1}^{(2)}}{\partial t} + \sigma E_{r,1}^{(2)}, \quad (5.76)$$

$$\frac{1}{r} \frac{\partial (r H_{\phi,1}^{(2)})}{\partial r} - \frac{1}{r} H_{r,1}^{(1)} = \varepsilon \varepsilon_0 \frac{\partial E_{z,1}^{(2)}}{\partial t} + \sigma E_{z,1}^{(2)}, \quad (5.77)$$

$$\frac{\partial E_{r,1}^{(2)}}{\partial z} - \frac{\partial E_{z,1}^{(2)}}{\partial r} = -\mu \mu_0 \frac{\partial H_{\phi,1}^{(2)}}{\partial t}, \quad (5.78)$$

$$\frac{\partial H_{r,1}^{(1)}}{\partial z} - \frac{\partial H_{z,1}^{(1)}}{\partial r} = \varepsilon \varepsilon_0 \frac{\partial E_{\phi,1}^{(1)}}{\partial t} + \sigma E_{\phi,1}^{(1)}, \quad (5.79)$$

$$-\frac{1}{r} E_{z,1}^{(2)} - \frac{\partial E_{\phi,1}^{(1)}}{\partial z} = -\mu \mu_0 \frac{\partial H_{r,1}^{(1)}}{\partial t}, \quad (5.80)$$

$$\frac{1}{r} \frac{\partial (r E_{\phi,1}^{(1)})}{\partial r} - \frac{1}{r} E_{r,1}^{(2)} = -\mu \mu_0 \frac{\partial H_{z,1}^{(1)}}{\partial t}. \quad (5.81)$$

The system of equations (5.76)–(5.81) can be approximately solved by the finite-difference method on the Yee sampling grid [18], but in a cylindrical coordinate system (Fig. 5.29) as in [82].

The finite-difference approximation of equations (5.76)–(5.81) has the form ( $\sigma = 0, \mu = 1$ ):

$$\begin{aligned} & \varepsilon(i + \frac{1}{2}, j) \varepsilon_0 \frac{E_{r,1}^{(2)n+1}(i + \frac{1}{2}, j) - E_{r,1}^{(2)n}(i + \frac{1}{2}, j)}{\Delta t} = \\ & = -\frac{1}{r(i + \frac{1}{2})} H_{z,1}^{(1)n+\frac{1}{2}}(i + \frac{1}{2}, j) - \frac{H_{\phi,1}^{(2)n+\frac{1}{2}}(i + \frac{1}{2}, j + \frac{1}{2}) - H_{\phi,1}^{(2)n+\frac{1}{2}}(i + \frac{1}{2}, j - \frac{1}{2})}{\Delta z}, \end{aligned} \quad (5.82)$$

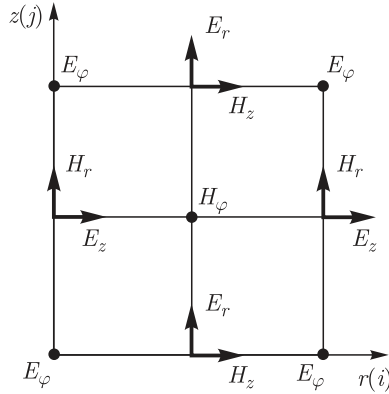


**Fig. 5.29.** Yee grid with a half-step in the cylindrical coordinates:  $h$  is the step in the spatial coordinates.

$$\begin{aligned}
 \varepsilon(i, j) \varepsilon_0 \frac{E_{\varphi,1}^{(1)n+1}(i, j) - E_{\varphi,1}^{(1)n}(i, j)}{\Delta t} &= \\
 = \frac{H_{r,1}^{(1)n+\frac{1}{2}}\left(i, j + \frac{1}{2}\right) - H_{r,1}^{(1)n+\frac{1}{2}}\left(i, j - \frac{1}{2}\right)}{\Delta z} - \frac{H_{z,1}^{(1)n+\frac{1}{2}}\left(i + \frac{1}{2}, j\right) - H_{z,1}^{(1)n+\frac{1}{2}}\left(i - \frac{1}{2}, j\right)}{\Delta r}, &
 \end{aligned} \tag{5.83}$$

$$\begin{aligned}
 \varepsilon\left(i, j + \frac{1}{2}\right) \varepsilon_0 \frac{E_{z,1}^{(2)n+1}\left(i, j + \frac{1}{2}\right) - E_{z,1}^{(2)n}\left(i, j + \frac{1}{2}\right)}{\Delta t} &= \\
 = \frac{1}{r(i)} \frac{r\left(i + \frac{1}{2}\right) H_{\varphi,1}^{(2)n+\frac{1}{2}}\left(i + \frac{1}{2}, j + \frac{1}{2}\right) - r\left(i - \frac{1}{2}\right) H_{\varphi,1}^{(2)n+\frac{1}{2}}\left(i - \frac{1}{2}, j + \frac{1}{2}\right)}{\Delta r} & \\
 - \frac{1}{r(i)} H_{r,1}^{(1)n+\frac{1}{2}}\left(i, j + \frac{1}{2}\right), &
 \end{aligned} \tag{5.84}$$

$$\begin{aligned}
 -\mu_0 \frac{H_{\varphi,1}^{(2)n+\frac{1}{2}}\left(i + \frac{1}{2}, j + \frac{1}{2}\right) - H_{\varphi,1}^{(2)n-\frac{1}{2}}\left(i + \frac{1}{2}, j + \frac{1}{2}\right)}{\Delta t} &= \\
 = \frac{E_{r,1}^{(2)n}\left(i + \frac{1}{2}, j + 1\right) - E_{r,1}^{(2)n}\left(i + \frac{1}{2}, j\right)}{\Delta z} - \frac{E_{z,1}^{(2)n}\left(i + 1, j + \frac{1}{2}\right) - E_{z,1}^{(2)n}\left(i, j + \frac{1}{2}\right)}{\Delta r}, &
 \end{aligned} \tag{5.85}$$

$$-\mu_0 \frac{H_{r,1}^{(1)n+\frac{1}{2}}\left(i, j+\frac{1}{2}\right) - H_{r,1}^{(1)n-\frac{1}{2}}\left(i, j+\frac{1}{2}\right)}{\Delta t} = \frac{1}{r(i)} E_{z,k}^{(2)n}\left(i, j+\frac{1}{2}\right) - \frac{E_{\phi,1}^{(1)n}(i, j+1) - E_{\phi,1}^{(1)n}(i, j)}{\Delta z}, \quad (5.86)$$

$$-\mu_0 \frac{H_{z,1}^{(1)n+\frac{1}{2}}\left(i+\frac{1}{2}, j\right) - H_{z,1}^{(1)n-\frac{1}{2}}\left(i+\frac{1}{2}, j\right)}{\Delta t} = \frac{1}{r\left(i+\frac{1}{2}\right)} \frac{r(i+1)E_{\phi,1}^{(1)n}(i+1, j) - r(i)E_{\phi,1}^{(1)n}(i, j)}{\Delta r} - \frac{1}{r\left(i+\frac{1}{2}\right)} E_{r,1}^{(2)n}\left(i+\frac{1}{2}, j\right), \quad (5.87)$$

where  $\Delta t$ ,  $\Delta z$ ,  $\Delta r$  are the discrete steps in the corresponding coordinates:  $z = i \Delta z$ ,  $r = j \Delta r$ ;  $t = n \Delta t$ . Moreover, the readings of electrical components are calculated in the whole times  $t = n \Delta t$ , and the readings of the magnetic vectors are computed at half-time points  $t = (n + 1/2) \Delta t$ . Equations (5.82)–(5.87) are an example of a conditionally stable difference scheme, which is solved by the sweep method with the boundary conditions. For stable convergence of the solutions of the system (5.82)–(5.87) discretization steps should be chosen to satisfy the inequality [82]:

$$c \Delta t \leq \Delta r / k, \quad \Delta r = \Delta z, \quad (5.88)$$

where  $c$  is the speed of light in vacuum,  $k$  is the number of angular harmonics of the equations (5.54), (5.55).

Note that the system (5.82), (5.87) differs from a similar system in [82] not only by the fact that in the system (5.82)–(5.87)  $k = 1$ , and in [82]  $k$  is arbitrary, but also by the fact that in [82] there are some errors in some signs in the system of equations (5.82)–(5.87).

### 5.3.5. Maxwell's equations for azimuthal polarization

If the optical element with axial symmetry (optical axis  $z$  is the axis of symmetry) received a normally incident electromagnetic monochromatic wave with azimuthal polarization (Fig. 5.28b), then at the electric vector there is only a single projection:

$$E^{\text{inc}} = E_{\phi} = E_0(r) \cos \omega t. \quad (5.89)$$

In the notations of (5.54) at the electric vector of the incident wave there is only one Fourier component (angular harmonic):  $E^{\text{inc}} = E_{\phi,0}$ . Therefore, in the system of equations (5.62)–(5.73) for the case of azimuthal polarization there are only three equations:

$$\frac{\partial H_{r,0}}{\partial z} - \frac{\partial H_{z,0}}{\partial r} = \varepsilon \varepsilon_0 \frac{\partial E_{\phi,0}}{\partial t} + \sigma E_{\phi,0}, \quad (5.90)$$

$$-\frac{\partial E_{\phi,0}}{\partial z} = -\mu \mu_0 \frac{\partial H_{r,0}}{\partial t}, \quad (5.91)$$

$$\frac{1}{r} \frac{\partial (r E_{\phi,0})}{\partial r} = -\mu \mu_0 \frac{\partial H_{z,0}}{\partial t}. \quad (5.92)$$

The difference approximation of the system (5.90)–(5.92) for the azimuthal polarization takes the form ( $\sigma = 0, \mu = 1$ ):

$$\varepsilon(i,j)\varepsilon_0 \frac{E_{\phi,0}^n(i,j) - E_{\phi,0}^{n-1}(i,j)}{\Delta t} = \frac{H_{r,0}^{n-\frac{1}{2}}\left(i, j + \frac{1}{2}\right) - H_{r,0}^{n-\frac{1}{2}}\left(i, j - \frac{1}{2}\right)}{\Delta z} - \frac{H_{z,0}^{n-\frac{1}{2}}\left(i + \frac{1}{2}, j\right) - H_{z,0}^{n-\frac{1}{2}}\left(i - \frac{1}{2}, j\right)}{\Delta r}, \quad (5.93)$$

$$-\mu_0 \frac{H_{r,0}^{n+\frac{1}{2}}\left(i, j + \frac{1}{2}\right) - H_{r,0}^{n-\frac{1}{2}}\left(i, j + \frac{1}{2}\right)}{\Delta t} = -\frac{E_{\phi,0}^n(i, j+1) - E_{\phi,0}^n(i, j)}{\Delta z}, \quad (5.94)$$

$$-\mu_0 \frac{H_{z,0}^{n+\frac{1}{2}}\left(i + \frac{1}{2}, j\right) - H_{z,0}^{n-\frac{1}{2}}\left(i + \frac{1}{2}, j\right)}{\Delta t} = \frac{1}{r\left(i + \frac{1}{2}\right)} \frac{r(i+1)E_{\phi,0}^n(i+1, j) - r(i)E_{\phi,0}^n(i, j)}{\Delta r}. \quad (5.95)$$

Note that the equations (5.90)–(5.92) and (5.93)–(5.95) were not considered in [82].

### 5.3.6. Maxwell's equations for radial polarization

If the optical element the axis of symmetry which coincides with the optical axis, receives a normally incident electromagnetic monochromatic wave with radial polarization (Fig. 5.28c), then the electric vector of the incident wave has only one radial component:

$$E^{\text{inc}} = E_r = E_0(r) \cos \omega t \quad (5.96)$$

or in the notation of equation (5.54):  $E^{\text{inc}} = E_{r,0}$ . Then only the following three of the six equations (5.76)–(5.81) remain for radial polarization:

$$-\frac{\partial H_{\phi,0}}{\partial z} = \varepsilon \varepsilon_0 \frac{\partial E_{r,0}}{\partial t} + \sigma E_{r,0}, \quad (5.97)$$

$$\frac{1}{r} \frac{\partial (r H_{\phi,0})}{\partial r} = \varepsilon \varepsilon_0 \frac{\partial E_{z,0}}{\partial t} + \sigma E_{z,0}, \quad (5.98)$$

$$\frac{\partial E_{r,0}}{\partial z} - \frac{\partial E_{z,0}}{\partial r} = -\mu \mu_0 \frac{\partial H_{\phi,0}}{\partial t}. \quad (5.99)$$

Finite-difference approximation of (5.97) - (5.99) has the form ( $\sigma = 0, \mu = 1$ ):

$$\varepsilon \left( i + \frac{1}{2}, j \right) \varepsilon_0 \frac{E_{r,0}^n \left( i + \frac{1}{2}, j \right) - E_{r,0}^{n-1} \left( i + \frac{1}{2}, j \right)}{\Delta t} = - \frac{H_{\phi,0}^{n-\frac{1}{2}} \left( i + \frac{1}{2}, j + \frac{1}{2} \right) - H_{\phi,0}^{n-\frac{1}{2}} \left( i + \frac{1}{2}, j - \frac{1}{2} \right)}{\Delta z}, \quad (5.100)$$

$$\begin{aligned} & \varepsilon \left( i, j + \frac{1}{2} \right) \varepsilon_0 \frac{E_{z,0}^n \left( i, j + \frac{1}{2} \right) - E_{z,0}^{n-1} \left( i, j + \frac{1}{2} \right)}{\Delta t} = \\ & = \frac{1}{r(i)} \frac{r \left( i + \frac{1}{2} \right) H_{\phi,0}^{n-\frac{1}{2}} \left( i + \frac{1}{2}, j + \frac{1}{2} \right) - r \left( i - \frac{1}{2} \right) H_{\phi,0}^{n-\frac{1}{2}} \left( i - \frac{1}{2}, j + \frac{1}{2} \right)}{\Delta r}, \end{aligned} \quad (5.101)$$

$$\begin{aligned} & -\mu_0 \frac{H_{\phi,0}^{n+\frac{1}{2}} \left( i + \frac{1}{2}, j + \frac{1}{2} \right) - H_{\phi,0}^{n-\frac{1}{2}} \left( i + \frac{1}{2}, j + \frac{1}{2} \right)}{\Delta t} = \frac{E_{r,0}^n \left( i + \frac{1}{2}, j + 1 \right) - E_{r,0}^n \left( i + \frac{1}{2}, j \right)}{\Delta z} \\ & - \frac{E_{z,0}^n \left( i + 1, j + \frac{1}{2} \right) - E_{z,0}^n \left( i, j + \frac{1}{2} \right)}{\Delta r}. \end{aligned} \quad (5.102)$$

Note that the equations (5.100)–(5.102) are not considered in [82]. Other features of the FDTD method for the case of cylindrical symmetry: calculations of fields on the optical axis at  $r = 0$ , and compliance with the boundary conditions in the form of perfectly absorbing layers, taken from [82]. The above-described radial FDTD method has been implemented in the programming environment Matlab 7.0.

### 5.3.7. Modeling the focusing of a plane linearly polarized wave by a spherical microlens

Consider the focus area of a plane axial wave with linear polarization incident on the flat surface of a plano-convex spherical microlens (Fig. 5.30).

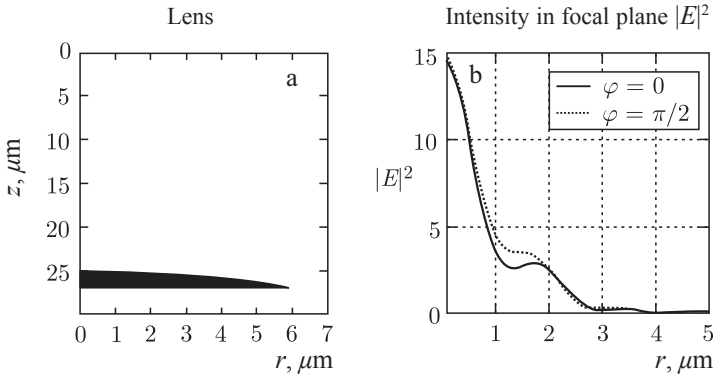


**Fig. 5.30.** Radial section of a plano-convex spherical microlens (a) and radial intensity distribution in the focal plane (b): curve 1, with  $\phi = 0$ , curve 2 at  $\phi = \pi/2$ .

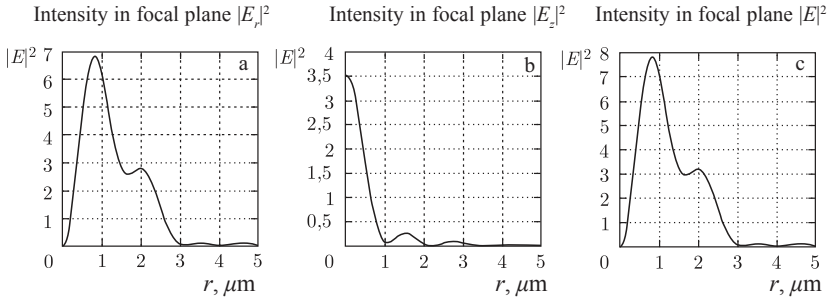


**Fig. 5.31.** The radial intensity distribution  $|E_r|^2$  (a),  $|E_z|^2$  (b) and  $|E_r|^2 + |E_z|^2$  (c) in the focus of the lens (Fig. 5.30a) upon impact by a plane wave with radial polarization

Figure 5.30a shows the radial cross section of the microlens: the lens aperture radius of  $6 \mu\text{m}$ , the radius of curvature of the spherical surface  $10 \mu\text{m}$ , the refractive index 1.5, the optical thickness of the lens on the optical axis  $2 \mu\text{m}$ . Wavelength  $1 \mu\text{m}$ . The discreteness of the spatial coordinates of  $1/20 \mu\text{m}$ , and the time coordinate  $1/40c$  s. Figure 5.30b shows the radial intensity distribution  $I = |E|^2 = |E_r|^2 + |E_\phi|^2$  in the focus on the horizontal  $x$  ( $\phi = 0$ ) and the vertical  $y$  ( $\phi = \pi/2$ ) axes. The focus is at the distance of  $11 \text{ mm}$  from the flat surface of the lens. Figure 5.30b shows that the focal spot has a weak ellipticity (eccentricity of the ellipse around 0.97). The long axis of the ellipse is directed along the axis  $y$  (polarization axis), and the short axis – along the axis  $x$ . The average diameter of the spot intensities at half intensity is  $\text{FWHM} = (d_x + d_y)/2 = 1.5\lambda$ . The area of the focal spot at half intensity is  $\text{HMA} = 1.77\lambda^2$ . The diameter of the spot means the full width of the intensity curve at half intensity???

Figure 5.31 shows the radial intensity distribution at the focus of the same lens (Fig. 5.30a), but upon impact by the radially-polarized plane wave whose electric vector has only one radial component  $E^{\text{inc}} = E_r$ . Figure 5.31 shows that the numeri-

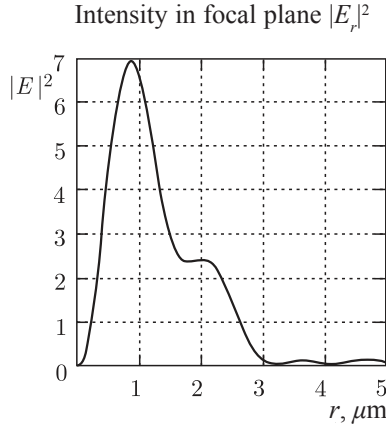


**Fig. 5.32.** The radial distribution of intensity  $|E_r|^2 = |E_\phi|^2$  in the focal plane of the lens (Fig. 5.30a) upon impact by a plane wave with azimuthal polarization.

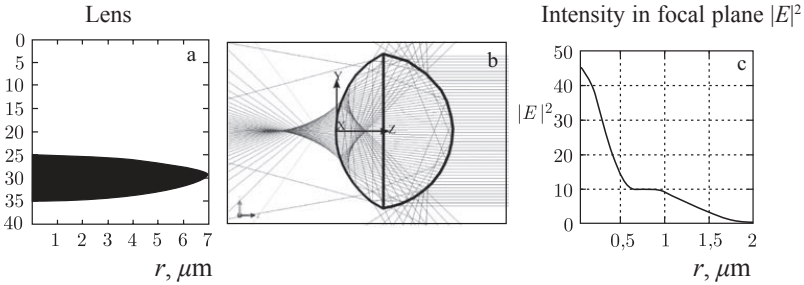
cal aperture of the lens (Fig. 5.30a) is not large enough to ensure that the intensity of the longitudinal component (Fig. 5.31b) exceeds the intensity of the radial component (Fig. 5.31a) to such an extent that the maximum at full intensity distribution (Fig. 5.31c) forms on the optical axis ( $r = 0$ ). Note that in the case of the radially-polarized light field at focusing through a radially symmetric optical element the amplitude of the radial component of the electric field strength on the optical axis is always zero:  $E_r(r = 0) = 0$ .

Figure 5.32 shows the radial distribution of the total intensity  $|E_r|^2 = |E_\phi|^2$  of the (there are no other projections at the electric vector in this case) when a plane wave with an azimuthal projection falls on the lens (Fig. 5.30a). It is evident that an annular intensity distribution with a zero on the optical axis forms in the focus.

Plano-convex spherical lenses has a maximum numerical aperture equal to  $\text{NA}_0 = (n^2 - 1)^{1/2}/n = 0.745$ . This limitation arises due to total internal reflection of light inside the lens. Therefore, half of the maximum angle of convergence of the rays at the focus is  $48^\circ$  (at  $n = 1.5$  – refractive index of the lens). To achieve maximum numerical aperture  $\text{NA}_0$  it is necessary to ensure that the aperture radius  $R_0$  of the plano-convex spherical lens is equal to  $R_0 = R_1/n$ , where  $R_1$  is the radius of curvature of the spherical surface. In this case,  $R_1 = 10 \mu\text{m}$ , so  $R_0 = 6.4 \mu\text{m}$ . The radius of the lens aperture in Fig. 5.30a is  $R = 6 \mu\text{m}$ , which is close to the maximum value of  $R_0$ . However, when the aperture radius (for a given radius of curvature  $R_1$ ) approaches the maximum value of  $R_0$  the focal spot is not reduced due to aberrations. In biconvex spherical lenses the numerical aperture can reach unity.

### 5.3.8. Focusing the light by biconvex spherical microlenses

Consider focusing of a plane wave with radial polarization by a biconvex spherical microlens. The lens parameters (Fig. 5.33a): the radii of curvature  $R_1 = 8.125 \mu\text{m}$ ,  $R_2 = 7.08 \mu\text{m}$ , the aperture radius  $R = 7 \mu\text{m}$ , thickness of the lens at the optical axis



**Fig. 5.33.** Lenticular spherical microlens (a), the rays in a lens (software TracePro) (b) and radial distribution of intensity  $|E|^2 = |E_r|^2 + |E_z|^2$  in the focal plane (c) in incidence of a plane wave with radial polarization,

$d = 10$  mm, the refractive index  $n = 1.5$ . The wavelength  $\lambda = 1$   $\mu\text{m}$ .

Although the diameter of the focal spot at the chosen radii of curvature  $R_1$  and  $R_2$  of the spherical surfaces (Fig. 5.33c) minimum (while maintaining the aperture radius  $R$ ), the energy efficiency of such a lens is about 50%. Figure 5.33b shows the rays passing through the lens (Fig. 5.33a), constructed with the help of TracePro commercial software. It is seen that only the rays that fall inside the lens enter the focal region. The remaining rays, due to total internal reflection, come out of the lens in other directions. The maximum angle at which the optical axis come to the focal point of the rays, is about  $60^\circ$  (half angle). That is the numerical aperture of the lens (Fig. 5.33a) is about  $\text{NA} = \sin(60) = 0.86$ . This is almost two times greater than the NA for the lens shown in Fig. 5.30a. The diameter of the focal spot at half intensity (Fig. 5.33c) is  $\text{FWHM} = 0.78\lambda$ . The total diameter (twice the distance from the maximum to first minimum) is equal to  $1.4\lambda$ , and the area of the focal spot at half intensity is  $\text{HMA} = 0.48\lambda^2$ . Recall for comparison that the minimum (with  $\text{NA} = 1$ ) area of the Airy disk in the scalar paraxial case is smaller and equal to  $\text{HMA} = 0.204\lambda^2$ . Thus, due to aberrations of the spherical lens it is not possible to achieve the minimum diameter of the focal spot, for example, as in [57.73].

### 5.3.9. Focusing of a plane wave with radial polarization by a gradient cylindrical microlens

Consider the focus of a plane wave with radial polarization incident normally on a flat surface of a cylindrical gradient microlens (GL) [14]. The refractive index of the GL depends on the radial variable as follows:

$$n(r) = n_0 \text{ch}^{-1} \left[ \frac{\pi r}{2L} \right], \quad (5.103)$$

where  $n_0$  is the refraction index on the optical axis,  $L$  is thickness of the lens along the optical axis (the lens looks like a cylinder or a piece of the gradient fibre). Equation (5.103) differs from (5.24) only in notation and by the change of variable  $y$  to  $r$ . All

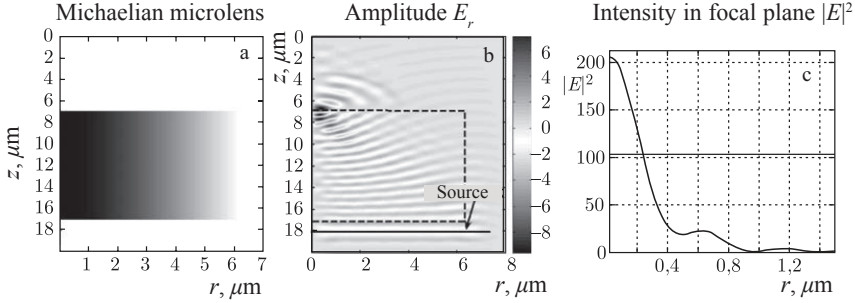


**Fig. 5.34.** The dependence of the refractive index on the radial coordinate in halftones for the GL (a) and the results of focusing: the instantaneous amplitude distribution  $E_r$  on the calculation field  $8 \times 20 \mu\text{m}$  (b), the radial distribution of intensity  $|E|^2 = |E_r|^2 + |E_z|^2$  in the focal plane (immediately behind the exit plane of the lens) (c).

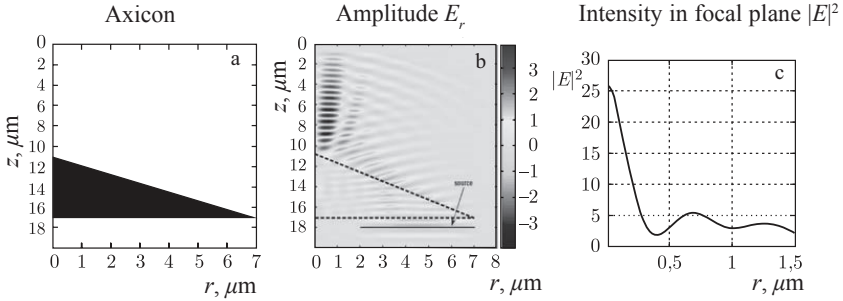
rays parallel to the optical axis and incident on the GL are collected in the focus at the optical axis on the opposite side of the lens. The microlens parameters (Fig. 5.34a):  $n_0 = 1.5$ ,  $L = 10 \mu\text{m}$ , the aperture radius of the lens  $R = 6 \mu\text{m}$ . The wavelength of light  $\lambda = 1 \mu\text{m}$ .

Figure 5.34a shows the radial distribution of the refractive index of the gradient microlens (5.103). The instantaneous field with the amplitude  $E_r$   $8 \times 20 \mu\text{m}$  in size shown in Fig. 5.34b. Figure 5.34c shows the radial distribution of the total intensity of the electric field  $|E|^2 = |E_r|^2 + |E_z|^2$  in the focal plane of the GL. The diameter of the focal spot at half intensity is  $\text{FWHM} = 0.44\lambda$ , and the radius from the maximum intensity to the first minimum is equal to  $0.45\lambda$ . The area of the focal spot at half intensity is  $\text{HMA} = 0.152\lambda^2$ . The area of this spot (Fig. 5.34c) is slightly lower than that obtained in [57] using a microlens with  $N = 0.9$  and a circular aperture ( $\text{HMA} = 0.160\lambda^2$ ), but slightly larger than the area of the focal spot obtained in [73] using a parabolic mirror ( $\text{HMA} = 0.134\lambda^2$ ). A gradient microlens (Fig. 5.34a) can be produced in the form of a binary photonic crystal [56].

### 5.3.10. Focusing of a Gaussian beam with radial polarization using a conical microaxicon

Consider the focusing of a Gaussian beam with radial polarization by a conical microaxicon (Fig. 5.35a). The axicon parameters: the radius of the circular base of the cone (aperture radius)  $R = 7 \mu\text{m}$ , the thickness of the axicon (cone height)  $d = 6 \mu\text{m}$ , the refractive index  $n = 1.5$ . The wavelength  $\lambda = 1 \mu\text{m}$ , the radius of the waist of the Gaussian beam  $w = 7 \mu\text{m}$ .

Figure 5.35b shows the calculated instantaneous amplitude of the radial component of the electric field  $E_r$  on a platform with the size of  $8 \times 20 \mu\text{m}$  (vertical axis is  $z$ , the horizontal axis  $r$ ). The horizontal segment (source) shows the position of the waist of the Gaussian beam incident on the axicon. Figure 5.35c shows the radial distribution of intensity  $|E|^2 = |E_r|^2 + |E_z|^2$  in the focal plane of the axicon (next to its apex). The radius of the focal spot from the maximum intensity to the first



**Fig. 5.35.** Conical microaxicon (a), the instantaneous amplitude  $E_r$ , calculated on the  $8 \times 20 \mu\text{m}$  field (b) and radial distribution of intensity  $|E|^2 = |E_r|^2 + |E_z|^2$  in the focal plane of the axicon (next to its apex) (c).

minimum is equal to  $0.40\lambda$ , and the diameter of the focal spot at half intensity is equal to  $\text{FWHM} = 0.36\lambda$ . The area of the focal spot in Fig. 5.35c at half intensity is  $\text{HMA} = 0.101\lambda^2$ .

This area is less than the record value obtained in [73] ( $\text{HMA} = 0.134\lambda^2$ ). Note that the numerical aperture of the axicon in this case is not greater than  $\text{NA} = 0.65$ .

If the axicon (Fig. 5.35a) is illuminated with circular Gaussian beam  $\exp(-(r - r_0)^2/w^2)$  with radial polarization, where  $r_0 = 4.5 \mu\text{m}$  and  $a = 2.5 \mu\text{m}$  is the radius of the Gaussian beam, we find the record to date parameters of the focal spot: the area at half intensity  $\text{HMA} = 0.096\lambda^2$  and the diameter at half intensity  $\text{FWHM} = 0.35\lambda$ . Figure 5.36a shows the calculated radial intensity distribution at the focus of an axicon (Fig. 5.35a), illuminated with a circular Gaussian beam, and Fig. 5.36b shows in halftones the diffraction pattern in the focal plane (immediately after the apex of the cone) in the coordinates  $(x, y)$ .

One can also note a shortcoming of such sharp focusing of the laser beam using an axicon: a low energy efficiency. Figure 5.36a shows that the maximum intensity at the focus is only 20 relative units, which is 30 times smaller than the intensity at the focus of the GL (Fig. 5.34c) with the same radius of the aperture. This is because the axicon forms a focal region with an extended depth of field. For example, for the axicon in Fig. 5.36a the depth of field at half intensity intensity is  $3 \mu\text{m}$ , and for the GL in Fig. 5.34a it is only  $0.5 \mu\text{m}$ .

## 5.4. Three-dimensional photonic crystals

The three-dimensional photonic crystal refers to a three-dimensional periodically structured dielectric, which creates a periodically inhomogeneous distribution of dielectric permittivity in the space of the crystal. Such a modulation of dielectric permittivity leads to the formation of a band structure of the energy levels of photons. We can trace the analogy between photonic crystals and ordinary crystals. In a typical crystal ions (nuclei) of atoms are arranged in the three-dimensional lattice. This arrangement creates the three-dimensional periodic distribution of the electric potential. Under such a potential the energy levels of

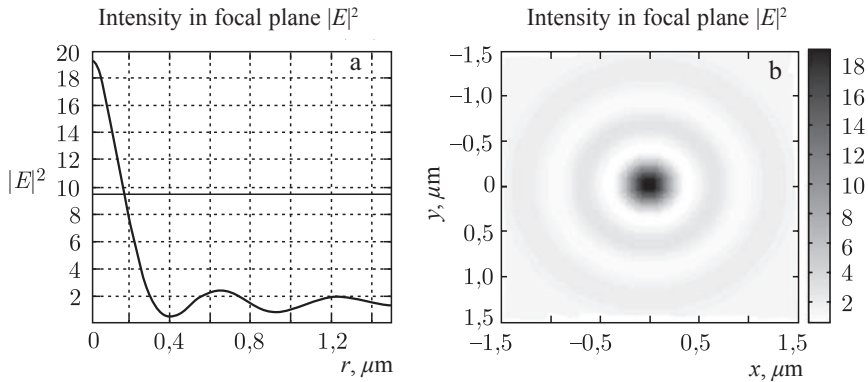


**Fig. 5.36.** The radial intensity distribution  $|E|^2 = |E_x|^2 + |E_z|^2$  in the focus of the microaxicon illuminated with a circular Gaussian beam with radial polarization, and the two-dimensional grayscale diffraction pattern (negative) in the focal plane in the coordinates  $(x, y)$  (b).

Crystal	Photonic crystal
Electrons	Photons
Atom lattice	Dielectric lattice
Periodically distributed potential	Periodically modulated dielectric permittivity

**Fig. 5.37.** Comparison of a conventional (electronic) crystal with a photonic crystal.

electrons are distributed in zones, in other words, the electron energy can only take certain values, corresponding to a certain energy level, just as it does in the potential well field. The potential in the crystal is infinite and periodic in space and in the potential well it is spatially limited, but both leads to the formation of energy levels. The analogue of the three-dimensional periodic potential modulation in a photonic crystal is the modulation of dielectric permittivity or refractive index. This modulation leads to discretization of the energy levels for electromagnetic waves, i.e. the emergence of the band structure for photons. For an electron in the potential well the optical analogue is not so close – it is an optical waveguide in which the restriction in the space of wave propagation in two coordinates leads to a discrete spectrum of wave vectors, rather than energy. The discrete spectrum of photon energies requires the three-dimensional localization or three-dimensional periodic modulation of the refractive index. The table in Fig. 5.37 shows some of the basic concepts similar for photon and conventional ‘electronic’ crystals,

The emergence of photonic band gaps can be visualized as follows. The three-dimensional periodic distribution of the dielectric leads to the situation in which the electromagnetic wave propagating in a certain direction is reflected in the structure as on a Bragg grating or a multilayer dielectric mirror. This ‘mirror’ reflects light only in a certain range of wavelengths, called the stop-band, whose position in the frequency spectrum depends on the grating period. If for all directions there is a range of overlap of the frequencies of the stop-bands, then this region forms a photonic band gap. Light with a wavelength belonging to this field can not propagate in any direction. Thus, an atom inside a photonic crystal can not emit light at this wavelength. Hence the threshold behaviour of the formation of the band gap on the basis of the magnitude of contrast of the dielectric permittivity of the grating becomes clear. The point is that different directions in the crystal correspond to different periodicity. Thus, the middle parts of the stop bands can be significantly shifted relative to each other in different directions – for example, for a square grating the periodicities along the diagonal of the cube are related as 1 to  $\sqrt{2}$ . To ensure overlapping of the stop-bands they should be made large enough. This is achieved by creating air–dielectric gratings from materials with a high refractive index. On the other hand, the overlap of stop-bands is best achieved at a more isotropic periodicity, i.e. in the form of the Brillouin zone, which is close to spherical.

The idea of controlling the spontaneous emission of atoms (the suppression of spontaneous emission of atoms) situated in a medium with three-dimensional periodic modulation of the refractive index was expressed in the papers by V.P. Bykov [83] in 1972. This possibility was then realized in 1987 by E. Yablonovich and S. John [9, 84] and the term ‘photonic crystal’ was suggested. Unlike an ordinary crystal, where the electron probability density wave is scalar, the electromagnetic wave field is of the vector nature. This required the development of new mathematical tools to calculate the band structure and led to a number of distinctive properties, in particular, the threshold nature of the band gap in the depth of modulation of the refractive index. In 1990 the band structure of photonic crystals was calculated for the first time and the photonic band gap was theoretically discovered [85]. Significant technological challenges in making photonic crystal gratings for the optical wavelength range have led to the fact that photonic crystals were first synthesized only in 2000, with these crystals having supposedly the band gap in the near infrared spectrum [86].

The first three-dimensional photonic crystal, in which the band gap was theoretically discovered, was a crystal with the symmetry of the diamond lattice, in which dielectric spheres were placed in the nodes [85]. The band gap was situated between the second and third zones. The band gap was then found in the FCC lattice structure formed by spherical cavities in a dielectric and located between the eighth and ninth bands [87]. The threshold of the existence of the band gap according to the refractive index of the first diamond lattice was 2.1 for the FCC lattice 2.8.

The requirement of a high refractive index of the structure limits the choice of material of the grating and significantly complicates the task of producing a photonic crystal. The table in Fig. 5.38 shows the refractive index for various materials.